# Light Matter Interactions: A Study of Soft Materials Using Linear and Nonlinear Spectroscopy

A Dissertation Presented for the

Doctor of Philosophy

Degree

The University of Tennessee, Knoxville

Muhammad Redwan Hassan

December 2022

# Acknowledgements

I would like to thank my advisor, Professor Tessa Calhoun for her guidance and support throughout my PhD journey. Her advice made me a better researcher and a better human being.

I would also like to thank my PhD committee members for their time and advice at different stages of the PhD program. My committee members include Professor Mark Dadmun, Professor Bhavya Sharma, and Professor Joshua Sangoro.

I would also like to acknowledge the support I got from my group members and friends here at UTK Knoxville. Without their support, it would have been a more difficult journey.

I would like to acknowledge the Department of Chemistry at the University of Tennessee for granting me the opportunity to do my PhD studies here and supporting me financially by providing a teaching assistantship. Lastly, I would like to acknowledge the support from the Department of Energy for funding the research project.

# Abstract

The adoption of complex fluids for various industrial applications is becoming normal. Complex fluids offer tunability, wide range solubility, and chemical and thermal stability which are the factors that conventional polar and non-polar solvents often lack. However, fundamental studies of these fluid systems are still lacking which is limiting the appropriate use of these complex fluids in many applications. The goal of this dissertation was to study and characterize complex fluids for application in electrolytes for redox flow batteries. Chapter 3 and chapter 4 feature the study of microemulsions and deep eutectic solvents (DES) by fluorescence techniques. Fluorescence studies of microemulsions revealed that the interfacial layer in the microemulsions, formed by the mix of surfactant and co-surfactant, can accommodate various small molecules diverse in structure. The hydration of the surfactant layer with the increase of water percentage beyond $< 60\%$ showed a sudden stiffening of the interfacial layer, which was reflected in the rotational time of the polar and ionic probes. The sudden stiffening of the surfactant region correlates to a morphological change in the microemulsion from bicontinuous to droplets. The fluorescence studies of DESs in chapter 4 revealed that the nonpolar probe molecule did not sense any environmental change with the increase of phenol content in the DES composition. The probe that senses the hydrogen bond network in their local environment revealed the existence of the hydrogen bond and also showed the weakening of its interaction at the higher phenol content in the DESs. Chapter 6 of this dissertation discusses the application of second harmonic generation spectroscopy to study the adsorption

of molecules at the charged surface and shows that nonionic surfactants differed in structure adsorb at the charged surface differently. The SHG tool can be leveraged in the future to screen potential surfactant molecules for applications in electrolytes.

# Table of Contents

# List of Tables

# List of Figures

# Chapter 1

# Introduction

## 1.1 Overview

In recent years, the adaptation towards green energy is increasing. Barth et al. (2022); Soloveichik (2015a) In general, feasibility and reliability of power grids producing electrical energy from solar and wind sources are limited by their energy storage systems. Soloveichik (2015a) Energy storage systems are a vital part of power grids because the renewable sources are intermittent which makes it difficult to ensure an uninterrupted distribution of electricity. Denholm et al. (2012) Modern fuel cells and lithium ion batteries are fulfilling a part of the demand, however, the high maintenance cost and small life cycle of these batteries make them an expensive solution to the existing problem. Zhao et al. (2015); Doughty et al. (2010) Redox flow batteries (RFB), once patented by NASA in 1981, Bartolozzi (1989) for large scale energy storage applications. Barth et al. (2022); Zhao et al. (2015); Soloveichik (2015a) The advantages of RFBs over conventional batteries comes from their modular design, durability and scalability properties, although low current density is limiting the application of the RFBs. Zhao et al. (2015) To overcome this problem, new classes of electroytes need to be developed which would have high current density and conductivity. To explore suitable solvent system for designing new electrolytes, microemulsions and deep eutectic solvents have been studied and the findings are summarized and discussed in this dissertation. Barth et al. (2022); Li et al. (2016)

## 1.2 Flow Battery and Electrolytes

In general, a battery is a device that mediates the conversion of chemical energy into electrical energy and vice-versa. Zhao et al. (2015) For large scale industrial applications RFBs are an ideal choice because of their design. Figure 1.1 shows the construction and working principle of RFB.

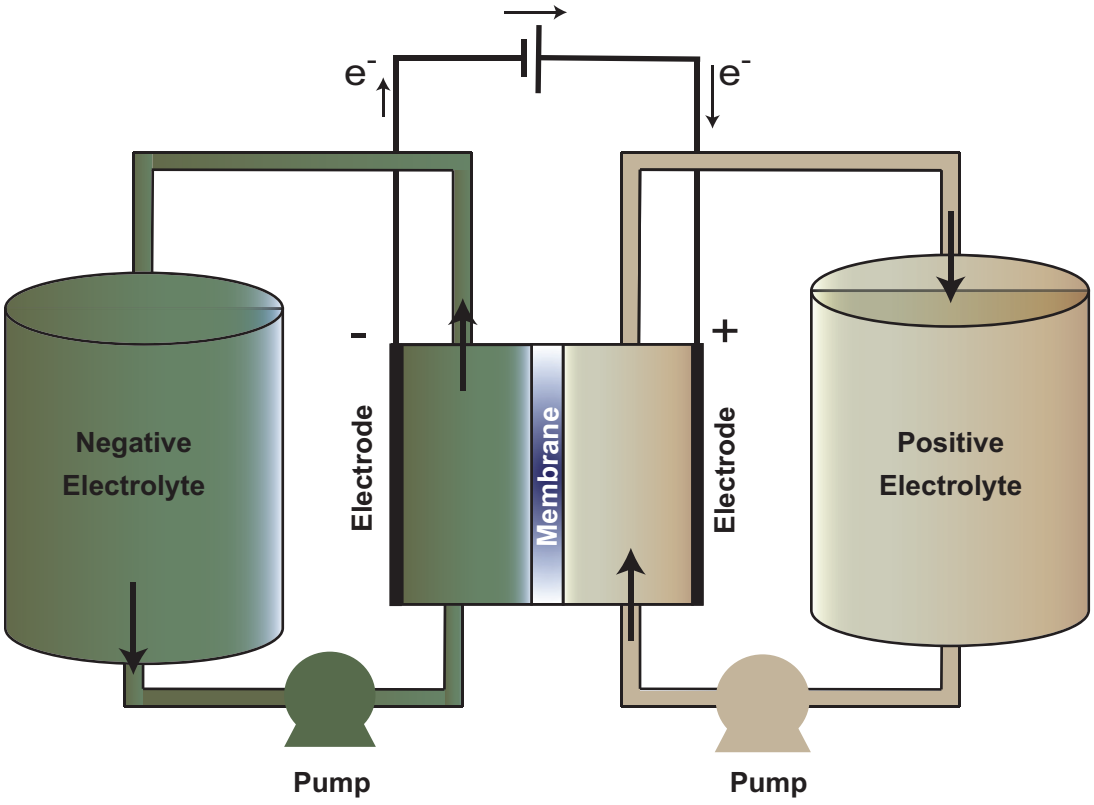


**Figure 1.1:** A schematic representation of the flow battery. The electrolyte from the tanks are pumped into the electrochemical cell.

This battery device consists of two parts: 1). the cell, where an ion exchange membrane separates the electrodes (cathode and anode), and 2). the electrolyte tanks, where electrolytes are stored. Weber et al. (2011) The basic difference between conventional batteries and RFBs is the presence of the electrolyte tanks in the latter, as in conventional batteries the electrolyte and the cell are not separated. In RFBs, electrolytes from the tanks are pumped into the cell. The redox pair dissolved in the electrolyte takes part in oxidation and reduction reactions at the electrode site. The electro-active agent gets oxidized at the anode, and electrons from the anode flow through an external circuit and reaches the cathode where the electro-active agent takes up the electron and gets reduced, in this process the battery gets discharged. The reverse process occurs when the battery is being charged. In the charging cycle, the electro-active agents at the aforementioned cathode donate an electron and get oxidized. The electron flows through the external circuit to the aforementioned anode section where the electro-active agent takes up the electron and gets reduced. Scalability of RFBs depends on the size of the tanks, as one can increase the capacity of the battery by simply making the tanks larger. Zhao et al. (2015) Although RFBs have many advantages over commercial energy storage systems, the low current density of RFB electrolytes is hurting its applicability in industries. Barth et al. (2022)

The RFB electrolytes are two types: 1) aqueous and 2) non-aqueous. Luo et al. (2019b) Aqueous electrolytes pose higher conductivity and favourable solubility of redox pairs which ensures higher energy and current density for RFBs. Luo et al. (2019a) However, the water dissociation potential limits the use of various aqueous redox pairs, limiting only to some metal ones. This is not the case for non-aqueous electrolytes, but the overall conductivity is low in this electrolytes because of their high viscosity. Luo et al. (2019b,b); Barth et al. (2022) Complex fluid systems, for example, microemulsions and deep eutectic solvents are being explored for RFB electrolyte applications. Imel et al. (2022); Barth et al. (2022); Mackay (1991) A brief introductory discussion about these complex fluids will be given in the following

sections. The main reasons for exploring these complex fluid systems is that these consist of aqueous and non aqueous domains which can facilitate the solubility of redox pairs and ensure high conductivity to achieve maximum current and energy density in electrolytes.

## 1.3 Microemulsions

Microemulsions are thermodynamically stable emulsions, consisting of water, oil, surfactants, co-surfactants and salts.Schramm (1992) In 1980, the use of microemulsion had spanned from laundry detergents to oil recovery in mining and refinery industries.McClements (2012) These days, their applications have expanded to drug delivery system, water purification, nanomaterial synthesis and food production.Israelachvili (1994); Rao and McClements (2011); McClements and Rao (2011) In recent times they are also being explored for electrolyte application as these fluids have the ability to solubilize polar and non-polar molecules.MacKay and Agarwal (1978); Peng et al. (2020)

The microemulsion was first introduced in 1943 by Hoar and Schulman. They reported a spontaneous formation of a transparent solution made from a turbid emulsion of oil and water when a strong surface active agent was added. Hoar and Schulman (1943) The study explained that the large emulsion drops divide into smaller droplets due to the sudden change of interfacial tension and interfacial energy at the interface of oil and water by the presence of the surfactant molecules, which made the solution visually transparent. Hoar and Schulman (1943) In 1959 Schulman coined the term "microemulsion" to name this system. Schulman et al. (1959) The size of the dispersed phases ranges from 5-100 nm in length but at the time when it was named, the smallest size imaginable was in the micron length scale. McClements (2012) Depending on the composition the dispersed domains can form oil in water, water in oil and bicontinous microemulsions.

Figure 1.2 shows a schematic of oil in water and bicontinuous microemulsions where the light blue background represents water, the light green is oil, and dark green molecules surrounding oil or forming the interface between oil and water are the surfactant and co-surfactant.

The amphiphilic surfactant molecules are made up of two parts; the head or hydrophilic region, and the tail or hydrophobic region, making them capable of solubilizing both polar and non-polar molecules. The stability of microemulsion comes from the presence of surfactant molecules forming the interface between oil and water. Israelachvili (1994) Microemulsion formation can be described using the Gibbs free energy equation.

$$\Delta G = \Delta A\gamma - T\Delta S \tag{1.1}$$

The term $\Delta S$ is configurational entropy change, which represents the entropy change due to the subdivision of the dispersed phase into droplets. G. Overbeek (1978) The term $\Delta A$ is the change in interfacial area arising from the formation of the smaller droplets. $\gamma$ is the interfacial tension between the oil and water phases and $T$ is the temperature in Kelvin. For the spontaneous formation of a microemulsion, the Gibbs free energy term $\Delta G$ needs to be negative and it can be achieved when $\Delta A\gamma$ becomes relatively smaller than $T\Delta S$. Kunieda and Shinoda (1980) The interfacial area of microemulsions is large compare to emulsions because the nanosize droplets have more surface area than the large emulsion droplets which makes the term $\Delta A$ large. Now for the spontaneous formation of microemulsion, $\gamma$ needs to be small, and it becomes small only when the interfacial tension between oil and water decreases significantly. Israelachvili (1994) In general, the interfacial tension between oil and water phases is about 50 $\mathrm{mNm}^{-1}$. McClements (2012) This interfacial tension can be altered by adding surfactant molecules. For instance, incorporating a double chain, ionic surfactant has proven to decrease the interfacial tension from a typical value of 50 $\mathrm{mNm}^{-1}$ to a $10^{-2}$.

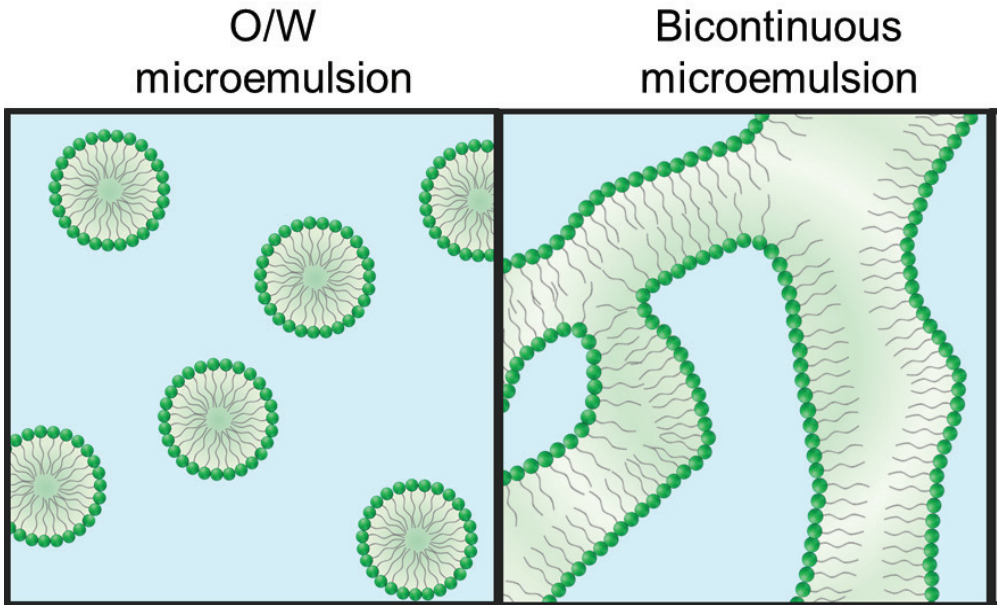


**Figure 1.2:** Different structures in microemulsion; droplets and bicontinuous

Alternatively, introducing a surfactant with a single non-ionic chain has been shown to decrease this value to $10^{-4}$ $mNm^{-1}$. Israelachvili (1994); McClements and Rao (2011); Sjöblom et al. (1996) To achieve lower interfacial tension, high concentrations of surfactant are often needed; however, this can lead to exceeding the critical micellar concentration (CMC). The CMC is the concentration at which the surfactant molecules do not adsorb at the interface between oil and water but rather forms micelles in the solvent. Evans et al. (1984) To circumvent this from occurring, medium chained alcohols, co-surfactants, are often used in addition to surfactants to reduce the interfacial tension between water and oil phases while maintaining a concentration of surfactant which is lower than its CMC. Evans et al. (1984); McClements and Rao (2011); Sjöblom et al. (1996)

In chapter 4 a microemulsion system made of Tween 20, butanol, water and toluene has been studied by using fluorescence techniques to observe small molecule sorting and structural changes in the microemulsions which are influenced by the variation of component loading.

## 1.4 Deep Eutectic Solvents

Deep eutectic solvents (DES) are formed from the eutectic mixtures of Lewis acids and bases with range of anionic and cationic species. Hansen et al. (2021); Smith et al. (2014) DESs were first introduced in 2001, in a study done by Abbott *et al.*Abbott et al. (2003) where he mixed powdered choline chloride and crystalline urea at 1:2 mole ratio and observed that the mixture turned liquid at room temperature. This was very significant because the melting point of the components of the mixture are around 302$^o$C (choline chloride) and 133$^o$C (urea) and the mixture made by mixing these solids turning into liquid was an unprecedented event. The sudden decrease of the mixture's melting point was believed to be caused by the formation of hydrogen bonds between the halide ion of the choline chloride and the hydrogen-donor moiety of urea.Abbott et al. (2003) The resulting liquid was coined as a deep eutectic mixture,

thus becoming the more common term, a DES. Abbott et al. (2003) DESs have been used in many industrial applications including pharmaceuticals, nanomaterial synthesis, metallurgy, gas separation, and catalysis.Abbott et al. (2006b,a); Hansen et al. (2021); Smith et al. (2014)

The formation of DESs can be described by the phase diagram shown in the Figure 1.3. In the figure, the melting points of the individual components $T_m(A)$ and $T_m(B)$ are labeled along the two y-axes. The opposites end of the x-axis represents the pure components A and B, and any point in the x-axis represents the exact molar ratio that develops a binary mixture. The lowest melting point found for a mixture in the phase diagram is the deep eutectic solvent.

DESs are divided into five categories defined by the type of the HBA and HBD molecules that make the final product. Hansen et al. (2021) Among those five categories, only the type III DES is explored as a sample of this research work. Type III DESs are made from the mixture of choline chloride and various HBD species that are organic molecules including alcohols, amides and carboxylic acids. Smith et al. (2014); Hansen et al. (2021) The range of HBD molecules that are available for the type III DESs, makes them versatile to implement in various applications including but not limited to biodiesel, metal processing, and cellulose derivatives synthesis. P. Abbott et al. (2007); Abbott et al. (2006a) Type III DESs can solvate a wide range of transitional metal ions, which is a very attractive characteristic for their application as electrolytes. Smith et al. (2014) Also these liquids are biodegradable, economical to synthesize, and unreactive to water. P. Abbott et al. (2007) Overall the ease of synthesis and favourable properties make Type III DESs ideal candidates to be considered while designing new classes of electrolytes. Hansen et al. (2021)

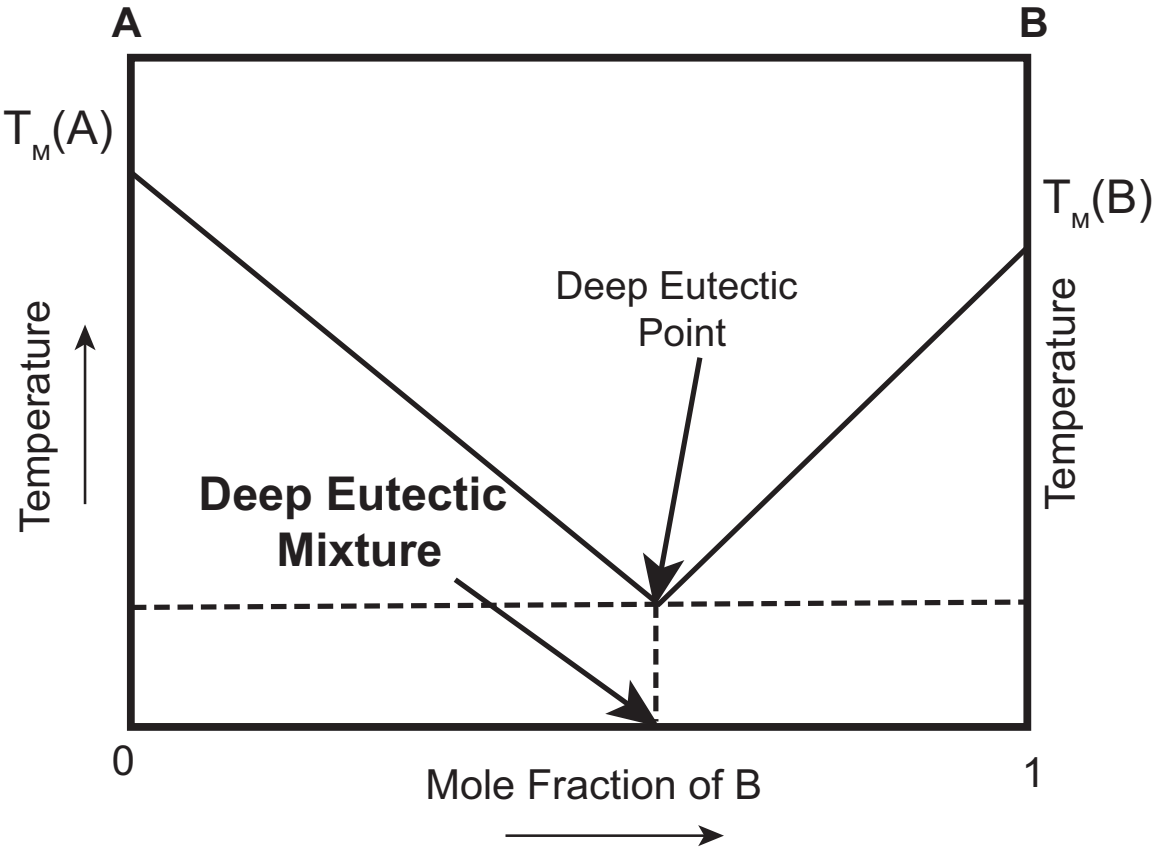


**Figure 1.3:** Phase diagram of DES formation, the melting point of the deep eutectic mixture is lower than the meting point of the neat components.

# Chapter 2

# Experimental Techniques

## 2.1 Light-Matter Interactions

This dissertation is based on the simple observations of the responses of matter to their interaction with light. When light interacts with a medium it induces a polarization $P$, Boyd (2020) which is defined by the following equation;

$$P = \epsilon_0(\chi^{(1)}E + \chi^{(2)}E^2 + \chi^{(3)}E^3 + ...) \tag{2.1}$$

Here $\epsilon$ is the permittivity of free space, $\chi^{(1)}$, $\chi^{(2)}$, and $\chi^{(3)}$ are the first, second and third order susceptibility tensor elements of the material, respectively, and $E$ is the electric field of the incident light. The overall induced polarization of the material depends on the numbers of photons interacting with the material. The first term in equation 2.1 describes linear optical processes resulting from a single electric field interacting with the matter. Examples of linear optical processes are absorption, fluorescence and phosphorescence. The subsequent terms in equation 2.1 describe the nonlinear optical processes, and can occur when more than one electric fields interact with the matter simultaneously. Boyd (2020)

Nonlinear optical processes include sum frequency generation, two-photon fluorescence, and third harmonic generation. When photons interact with matter, both linear and nonlinear processes can occur and the induced polarization of the matter is the sum of all the terms in equation 2.1. The terms in equation 2.1 mainly consists of two parts; 1) susceptibility tensors and 2) the electric field of incident light. The susceptibility tensors of higher terms are weaker than the lower terms ($\chi^{(1)} > \chi^{(2)} > \chi^{(3)}$) Boyd (2020), and because of that, the induced polarization of matter often dominated by the linear term. That is why for nonlinear optical process to occur, the incident electric field's strength needs to be very high. The interaction of incident electric fields of light with matter, and the resulting induced polarization change is a probabilistic process. As such, it is very rare for multi-photon events to occur in matter under standard conditions. Ultrashort laser pulses can provide the high photon densities necessary to increases the probability of multi-photon interaction

events occurring in matter. Material conditions are also required for nonlinear optical processes to occur. For example, second harmonic generation only occurs in non-centrosymmetric material because the second order susceptibility tensor is zero in symmetric material. Boyd (2020)

## 2.2 Linear Optical Processes

### 2.2.1 Fluorescence

Fluorescence is the emission of light from a molecule when it descends from the electronic excited state to its ground state without any change of its spin state. lak (2006a) The Jablonski diagram shown in Figure 2.1 schematically represents the processes of absorption and fluorescence by molecule upon its interaction with light. In the diagram thicker lines labeled $S_0$ and $S_1$ are electronic ground state and excited state of a molecule, respectively. The thinner lines above the electronic states represents the vibrational energy states. When molecules in the ground state $S_0$ interacts with photons of frequency $\omega_1$, they can absorb the light and transition to the higher electronic excited state, $S_1$. A molecule promoted to the $S_1$ state transfers its energy by internal conversion and relaxes down to the lowest vibrational energy level of $S_1$ before it relaxes back to the $S_0$ state by emitting a photon of frequency $\omega_2$. This linear optical process of conversion of a photon of frequency $\omega_1$ to a photon of frequency $\omega_2$ is called fluorescence. The time a molecule spends at the excited state is called its fluorescence lifetime which typically ranges from sub-nanoseconds to 10 ns ($10^{-9}$). The figure also reveals that the energy of fluorescence is of lower energy compared to the absorbed photon because part of the absorbed energy is dissipated through internal conversion via vibrational relaxation. The process by which molecules at the excited state dissipate energy other than fluorescence is known as nonradiative energy loss. Nonradiative energy loss includes internal conversion, thermalization, solvent interactions, energy transfer and quenching.

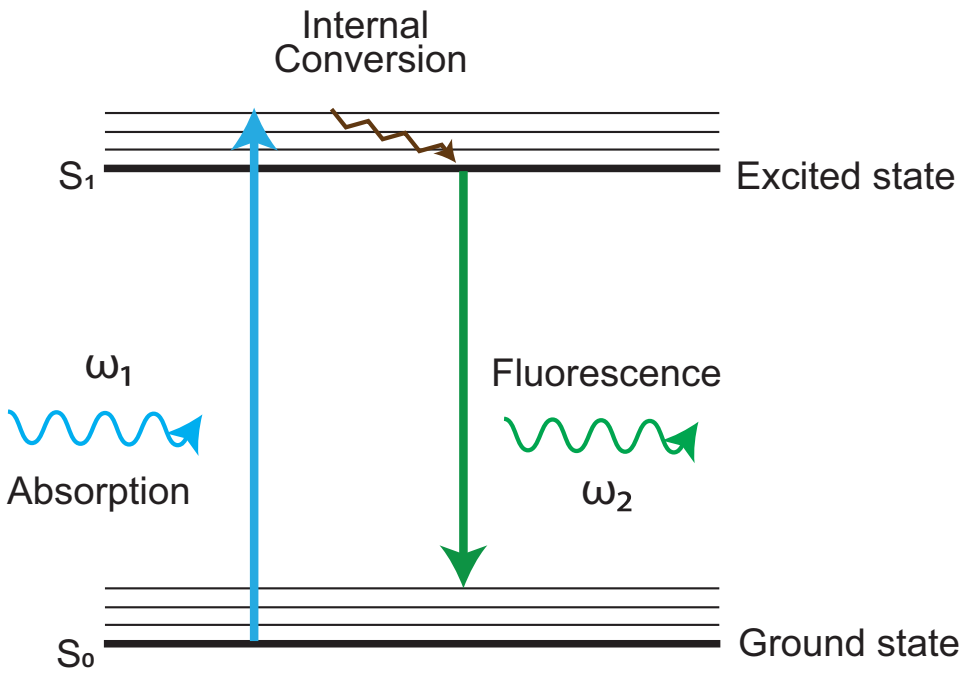


**Figure 2.1:** A Jablonski diagram showing the process of fluorescence

Fluorescence measurements are classified into two types: steady-state measurements and time-resolved measurements. Depending on the measurement type, information about fluorophore's (distinct organic molecules that have the capability to undergo fluorescence processes) size, solvent interaction, energy transfer and local environment microviscosity can be gathered. In chapter 3 and 4 the steady-state and time-resolved fluorescence measurements of fluorophores dissolved in microemulsions and deep eutectic solvents will be discussed.

### 2.2.2 Steady-State Fluorescence

In steady-state fluorescence measurements, samples are excited with a continuous-wave light source and fluorescence from the samples are recorded continuously as excitation/emission wavelengths are scanned. The results from steady-state fluorescence measurements show the average response of the bulk sample. Because of that, much of the sample information get buried through the averaging process. The steady-state fluorescence measurements include excitation and emission scans, steady-state fluorescence anisotropy, and Főrster resonance energy transfer (FRET) of fluorophores. As the steady-state measurement are the average of multiple single events, the signal of steady-state fluorescence depends on the concentration of fluorophore, the power of excitation and the sensitivity of the detectors.

### 2.2.3 Fluorescence Anisotropy

The fluorescence anisotropy, $r$, is defined by the ratio of the difference between polarized emission intensity and total emission intensity:

$$r = \frac{(I_{\parallel} - I_{\perp})}{(I_{\parallel} + 2I_{\perp})} \tag{2.2}$$

where $I_{\parallel}$, is the intensity of fluorescence of parallel polarized to the excitation polarization and, $I_{\perp}$ is the intensity of fluorescence of perpendicular polarized to the excitation polarization. Fluorescence anisotropy measurements are done by

selectively exciting the ground state molecules whose absorption transition moments align with the vertically polarized incident excitation light. The emission from the selectively oriented excited state population will also be polarized. Some of the molecules will emit polarized fluorescence; however, some of the molecules will get depolarized by rotational diffusion and emit randomly polarized light. The polarized emissions can be selectively collected through a polarizer which is aligned parallel or perpendicular with respect to the polarization of the excitation light. Inserting the parallel $I_{\parallel}$ and perpendicular $I_{\perp}$ polarized fluorescence intensity in the equation 2.2 the anisotropy value of the fluorophore in a sample is calculated. The theoretical anisotropy value should be free of depolarization but fluorophores get depolarized by rotational diffusion, solvent interaction and energy transfer. The fluorescence anisotropy value can be measured by steady-state fluorescence measurements, but to measure the rotational diffusion of fluorophores in a sample, time-resolved fluorescence anisotropy is required. Time resolved fluorescence anisotropy is defined by the following equations

$$r(t) = r_0 a e^{\frac{-t}{\tau}} \tag{2.3}$$

Here $r_0$ is the initial anisotropy, free of depolarization, and $t$ is the correlation time, which corresponds to the rate of rotational diffusion of the fluorophore and $r(t)$ is the anisotropy decay which is defined by,

$$r(t) = \frac{I_{\parallel}(t) - G I_{\perp}(t)}{I_{\parallel} + 2G I_{\perp}(t)} \tag{2.4}$$

$I_{\parallel}(t)$ and $I_{\perp}(t)$ in equation 2.4 are the parallel and perpendicular polarized fluorescence lifetime decays. $G$ is called the G factor and is defined as the ratio of the sensitivity of the detection system for vertical and horizontal polarized light. Time-resolved fluorescence anisotropy measurements require a pulsed excitation light source, fast photo detectors, and a single photon counting device. lak (2006b)

### 2.2.4 Instrumentation

In this thesis work, all the time-resolved fluorescence measurements were carried out on a home-built instrument. Figure 2.2 shows the schematic diagram of the instrument. Briefly, an Nd:YAG pumped Ti:Sapphire oscillator yielding <100 fs laser pulses at 800 nm was used as the excitation light source. The repetition rate of 80 MHz was modulated to 13.33 MHz with an electro-optic modulator. Light was focused into a $\beta$-barium borate (BBO) crystal for frequency doubling. The resulting 400 nm light was used to excite coumarin 153 (c153), 9,10- diphenylanthracence (DPA), and 4-aminophthalimide (4AP). Alternatively the light source was passed through a supercontinuum fiber (Newport FW800-0854) in place of the $\beta$-barium borate (BBO) crystal, the output from the fiber was filtered by a 530/55 nm bandpass filter to isolate 530 nm light which was used to excite rhodamine 6G (r6g). Before the light is focused on the the sample it is passed through a waveplate and a Glan-Taylor polarizer (excitation polarizer) to control the intensity and polarization of the excitation light. Vertical polarized light from the polarizer was focused onto the sample cuvette. The fluorescence from the sample was collected by a series of lens and passed through a second Glan-Taylor polarizer (emission polarizer) and bandpass emission filter (530/55 nm for c153, 475/25nm for DPA, 572/17 nm for r6g) before it was focused on to an avalanche photodiode. The data was acquired from the TCSPC by PicoHarp 300 software. The instrumental response was measured with an aqueous solution of 100 $\mu$M DASPMI Li et al. (2016) and was found to be $\sim$40 ps FWHM.

### 2.2.5 Calibration

Before beginning the anisotropy measurements of the microemulsion samples with the home-built instrument, a couple of control experiments were performed with c153 in butanol and r6g in water. The measured anisotropy values were compared with values that have been reported in the literature.

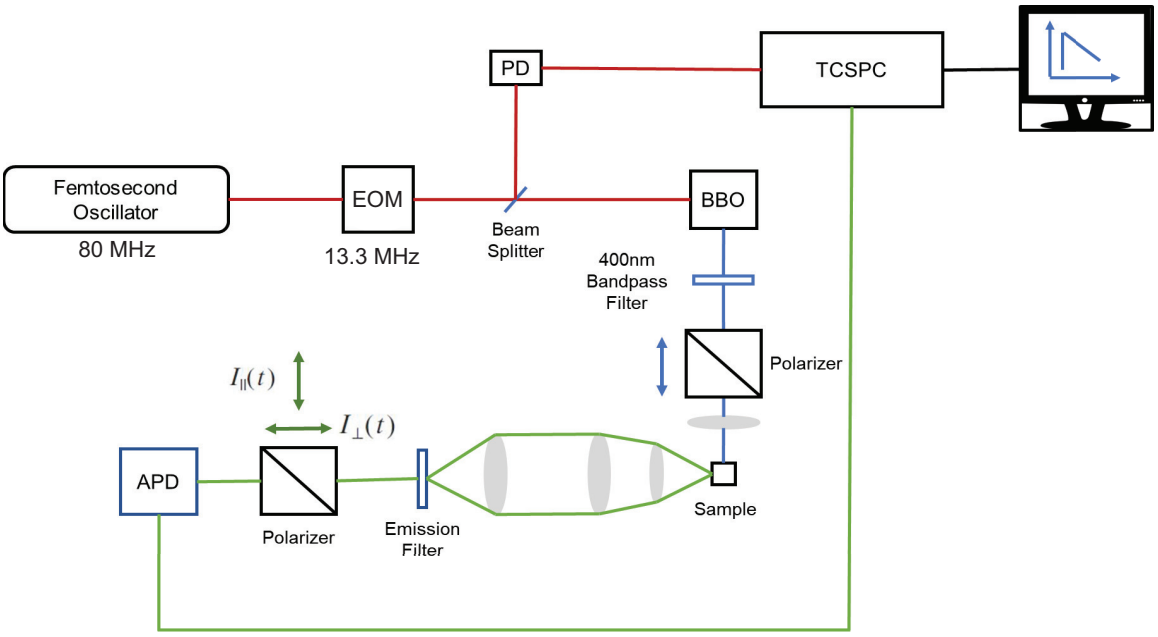


**Figure 2.2:** Homebuilt time-resolved fluorescence spectroscopy

The anisotropy value and the rotational time found from the control experiments of c153 in butanol and r6g in water were 0.369 ± 0.006 and 234.1 ± 3.7 ps, and 0.389 ± 0.005 and 251 ± 7.9 ps, respectively which was in agreement with the values reported in the literature.Horng et al. (1995); Gumy and Vauthey (1996)

## 2.3 Nonlinear Optical Processes

In nonlinear optical processes, the induced polarization of the material arises from the higher order terms in the equation 2.1. As discussed earlier, interaction of two or more incident electric fields with the matter is required for nonlinear optical processes. In this section, the basic principle and instrumentation of second harmonic generation (SHG) spectroscopy will be discussed.

### 2.3.1 Second Harmonic Generation

The Jablonski diagram shown in the Figure 2.3 can be used to describe the SHG process. When two photons of the same frequency, $\omega_1$, interacts with ground state molecules, the molecules are promoted to a virtual state. Boyd (2020) Virtual states are not real electronic states but representations of one of the eigenstates of the molecule. Upon relaxation from the virtual state, a molecule can convert those two photons of frequency $\omega_1$ into one photon of double frequency of $2\omega_1$. The material needs to be non-centrosymmetric for the second order nonlinear optical process to occur because the susceptibility tensors term, $\chi^{(2)}$, of symmetric molecules are zero. Interfaces or surfaces fulfil the non-centrosymmetric requirement as they inherently break the inversion symmetry of the bulk. Boyd (2020) This is why SHG spectroscopy techniques are ideal for the study of surfaces or interfaces buried in bulk systems. In chapter 5, SHG spectroscopy will be utilized to study the interaction of surfactants and charged particle surfaces.

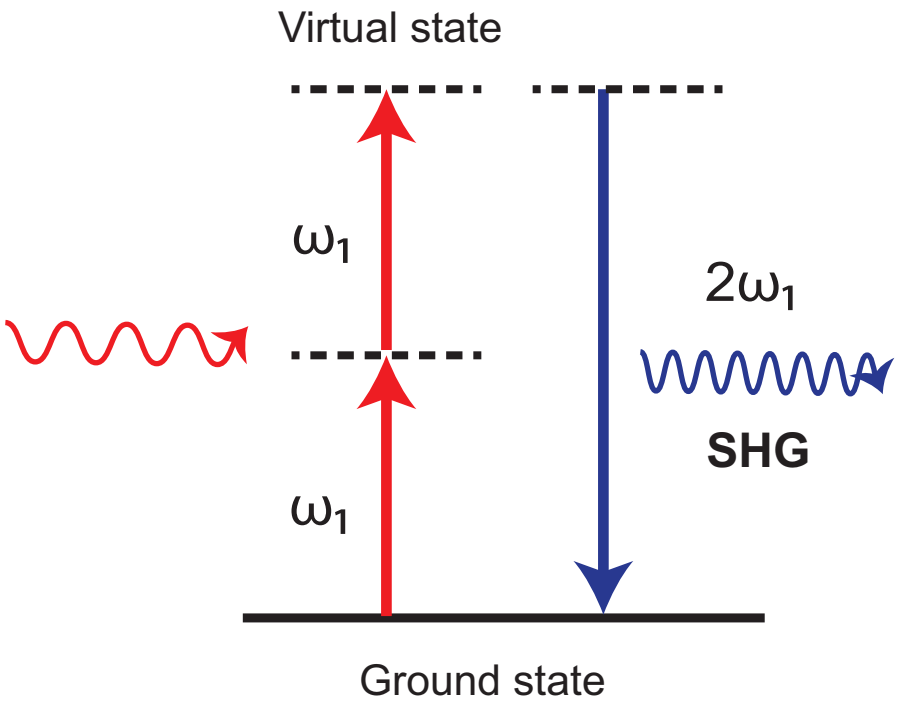


**Figure 2.3:** Jablonski diagram of Second Harmonic Generation

### 2.3.2 Instrumentation

To carry out the studies described in chapter 5, a home-built SHG spectroscopy instrument was used. Figure 2.4 shows the schematic view of instrument. An Nd:YAG pumped Ti:Sapphire oscillator (MaiTai from Spectra Physics) yielding <100 fs pulse center at 800 nm with the repetition rate of 80 MHz was utilized as the fundamental light for the SHG. The light was passed through a half- waveplate and a polarizer, which in combination functioned as a power attenuater for the light. The light was than passed through a 475 nm long pass filter to ensure that the light focusing on to the sample cuvette is free of any second harmonic light generated from the preceding optics. Coherent SHG scatter from the sample was collected by a series of lenses and focused onto an optical fiber. A 725 nm shortpass fiter was placed before the optical fiber to filter out the remaining fundamental light from the SHG signal. At the other end of the fiber, a detection setup consisting of a 400/10 nm bandpass filter and a photon counting PMT detector was placed. Home-built LabVIEW software was used to acquire data. Calibration of the setup was carried out by measuring the SHG signal arising from a sample containing SHG resonant malachite green (MG) dye molecules adsorbed to the polystyrene beads. The SHG signal from the sample was collected at different laser power and the signal was plotted as function of the output power of the fundamental light. Obtaining a square exponent after fitting the data with the SHG power law fit equation ensured proper performance.

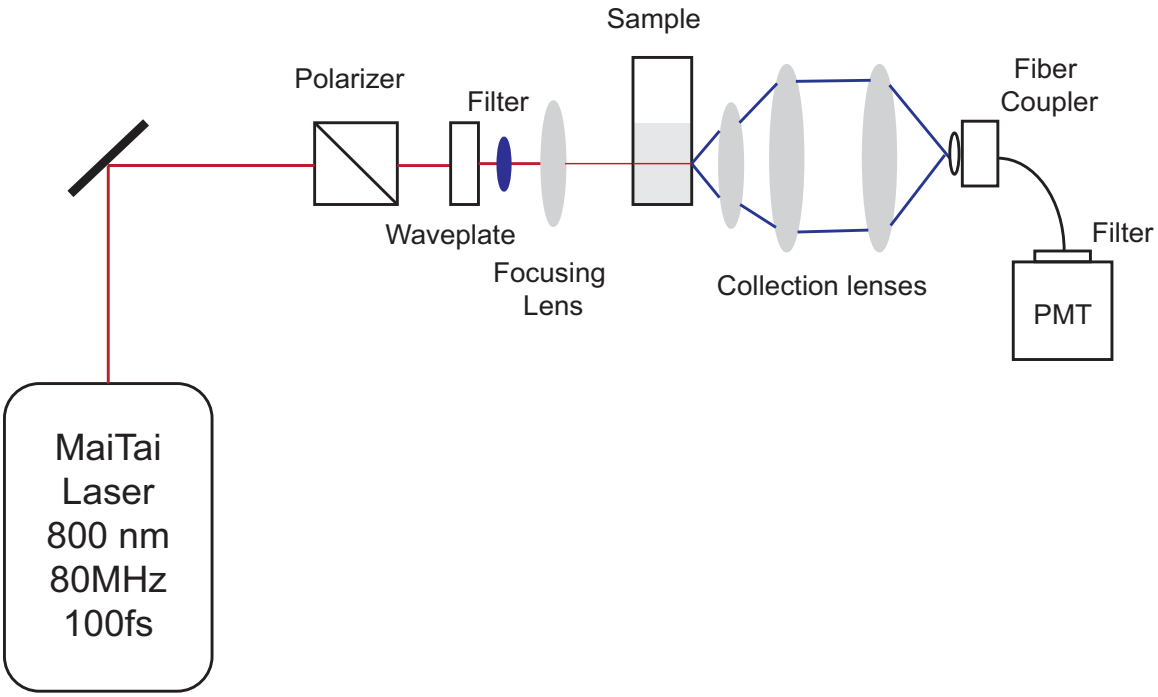


**Figure 2.4:** Diagram of Home-built SHG instrument

# Chapter 3

# Small molecule sorting: Fluorescence study of microemulsions

A version of this chapter has been reprinted from the Journal of Physical Chemistry B from:

Muhammad Redwan Hassan, Brandon A. Colon, James Russell, and Tessa R. Calhoun, "Small Molecule Sorting: A Fluorescence Study of Microemulsions," The Journal of Physical Chemistry B, 2022, 126, 26, 4990-4998 .



This chapter describes experimental design by myself and Tessa R. Calhoun. A part of instrumental alignment was performed by B.A. Colon. I completed all experiments, data, and figures. Data check software was designed by J. Russell. Data analysis was performed by myself and Tessa R. Calhoun. The manuscript was prepared by myself and Tessa R. Calhoun.

## 3.1 Abstract

The application of microemulsions to a wide range of industries relies on their ability to solubilize small molecules with vastly different structures. Herein, we use multiple fluorescence techniques to probe ionic (rhodamine 6g, r6g), polar (coumarin 153, c153), nonpolar (diphenylanthracene, DPA), and amphiphilic (laurdan) small molecules in a nonionic, bicontinuous microemulsion of varying hydration. All fluorophores investigated were found to associate with the surfactant region despite their different structures and properties. The hydration of the surfactant layer was found to increase linearly with water addition, but while this initially increases the fluidity of the surfactant layer, fluorescence anisotropy of c153 and r6g indicates a stiffening of the surfactant at water content >60%. This stiffening of the surfactant layer at higher water content correlates with a morphological change in the microemulsion from a bicontinuous structure to droplets. In contrast, the nonpolar DPA shows a change in partitioning as hydration changes increasing its association with the oil domain. Overall, these studies elucidate not only the capability of these microemulsions to host a range of small molecules in the surfactant layer with tunable position, but also the ability to probe the driving force of bulk structural changes in these heterogeneous fluids.

## 3.2 Introduction

Microemulsions are complex, heterogenous fluids with emergent properties that have enabled their use in a wide array of scientific and industrial applications, including oil recovery and oil spill cleanup, Reed et al. (1999); Schramm (1992) drug delivery systems, Sjöblom et al. (1996); Shakeel et al. (2010); Velikov and Pelan (2008); Huang et al. (2010) water purification,Stumm and Morgan (1996) emulsion polymerization,Chern (2006) nanomaterial synthesis, Ganguli et al. (2010); López-Quintela (2003) and bio-oil enhancement.Leng et al. (2018). In addition, their

ability to solubilize both aqueous and nonaqueous species has facilitated the use of microemulsions in many electrochemical systems MacKay and Agarwal (1978); Shah et al. (1997); Jha et al. (1995); Iwunze et al. (1990); Ying et al. (2009); Dayalan et al. (2002); Mackay (1991); Mackay et al. (1996); Kunitake et al. (2016); Rusling (2007), including flow batteries.Peng et al. (2020)

Microemulsions are water and oil suspensions stabilized by surfactants and cosurfactants. In contrast to standard emulsions, microemulsions are thermodynamically stable.Schulman et al. (1959) Depending on the identity and relative concentrations of oil, water, and the surfactant system, the constituent water and oil domains can range from droplets (oil-in-water dispersion or vice versa) to bicontinuous structures where continuous, worm-like domains of water and oil are separated by the surfactant monolayer.Strey (1994) Throughout this compositional tuning, microemulsions maintain transparency due to the sub-100 nm length scale of these domains.McClements (2012) Microemulsions can be made with ionic or nonionic surfactants, with the former more commonly studied. Singha et al. (2018); Chen et al. (1988); Shah et al. (1997); Lissi et al. (2000) The use of nonionic surfactants, however, ensures that electrolytes added to the aqueous phase have minimal to no effects on the behavior of the surfactant.Stevens (1957) This advantage of nonionic surfactants over ionic ones is an important consideration for applications in electrochemical systems.

An underlying question, arising from the applications listed above, remains regarding the location of different small molecules and their ability to move within, and potentially between, the domains of the heterogenous microemulsion environments. In this article, we focus on a microemulsion system composed of the nonionic surfactant Tween 20, the cosurfactant butanol, water, and toluene (TBWT). Previously, electrochemical reactivity in this TBWT microemulsion system was studied with an eye to its potential application in flow batteries.Peng et al. (2020) The rate of electron transfer observed was hypothesized to arise from the partitioning of both ionic and electroactive species into the interfacial surfactant region, as to be in close proximity. Extension of this work implicated the importance

of the diffusion of the electroactive species within and between microenvironments for its electrochemical performance.Shen et al. (2021) Herein, we explicitly test these hypotheses by probing the locations and mobilities of multiple small fluorescent probe molecules in different compositions of the TBWT microemulsion system with both steady-state and dynamic fluorescence spectroscopy techniques.

The use of fluorescence to study structural transitions in microemulsions dates back to 1988 when Chen *et al.* employed steady-state fluorescence anisotropy to study the curvature and geometric constraints in a microemulsion composed of didodecyldimethylammonium bromide surfactant, alkanes, and water.Chen et al. (1988) Since then, a variety of fluorescence techniques have been used to study many different aspects of microemulsions, including morphology/structural changes,Singha et al. (2018); Oliveira et al. (2001) small molecule localization,Oliveira et al. (2001); Lissi et al. (2000) surfactant hydration,Oliveira et al. (2001); Lissi et al. (2000) domain sizes and distributions,Khan et al. (2016); Pal et al. (2011) and rotational behavior of small molecules.Rao et al. (2012); Chakrabarty et al. (2005); Pramanik et al. (2010); Seth et al. (2006); Laia and Costa (2002). Herein, we employ both steady-state and time-resolved fluorescence spectroscopies to examine localization and dynamics. First, as the water content of the microemulsion was observed to significantly influence the electron transfer kinetics,Peng et al. (2020) we directly monitor the surfactant hydration using the generalized polarization (GP) of the amphiphilic probe, laurdan.Parasassi et al. (1994) Second, steady-state fluorescence spectroscopy was also used to determine the partitioning of an nonpolar probe, diphenylanthracene (DPA), a polar probe, coumarin 153 (c153), and the ionic probe, rhodamine 6g (r6g), as well as the relative proximity of the latter two. Finally, time-resolved fluorescence lifetimes and anisotropies were collected for the probes to assess their mobility. Overall, our results confirm that small molecules of different polarity reside in close proximity in the surfactant region, and, in addition, their dynamics can reflect larger structural changes in the microemulsions.

## 3.3 Materials and Methods

### 3.3.1 Chemicals

Polysorbate-20 (Tween 20), anhydrous 1-butanol, anhydrous toluene, methyl viologen and 9,10-diphenylanthracene were purchased from Fisher Scientific. Laurdan and rhodamine 6g were purchased from Thermo Fisher Scientific, and coumarin 153 was purchased from Exciton. All solvents and small molecule probes were used as received.

### 3.3.2 Microemulsion Preparation

Microemulsion samples were prepared according to the compositions given in Table 3.1. As can be seen in the ternary diagram in Figure 3.1, all compositions resulted in single phase microemulsions. The surfactant mix was made by adding 17.5 wt % butanol (cosurfactant) and 82.5 wt % polysorbate-20 (surfactant) to achieve the hydrophilic-lipophilic balance (HLB) to maximize the toluene solubility.Peng et al. (2020) The 1:10 oil to surfactant ratio was kept fixed for all samples. Deionized Milli-Q water was added as the final step in the preparation to achieve the desired water loading percentage in the microemulsions. The samples were then vortexed for 30 seconds. Sample names in Table 3.1 report the water percentages in the individual microemulsion samples. All of the measurements presented below were taken using freshly-prepared samples.

All probe molecules were dissolved in neat solution components before the microemulsions were formed. The amphiphilic chromophore laurdan was dissolved in butanol first, then the required amount of butanol with laurdan was mixed with Tween 20 to make the surfactant mix. The final concentration of laurdan was 5 $\mu$M in all microemulsion samples. C153 and DPA were dissolved in toluene, and r6g was dissolved in water before those components were incorporated into the microemulsion samples.

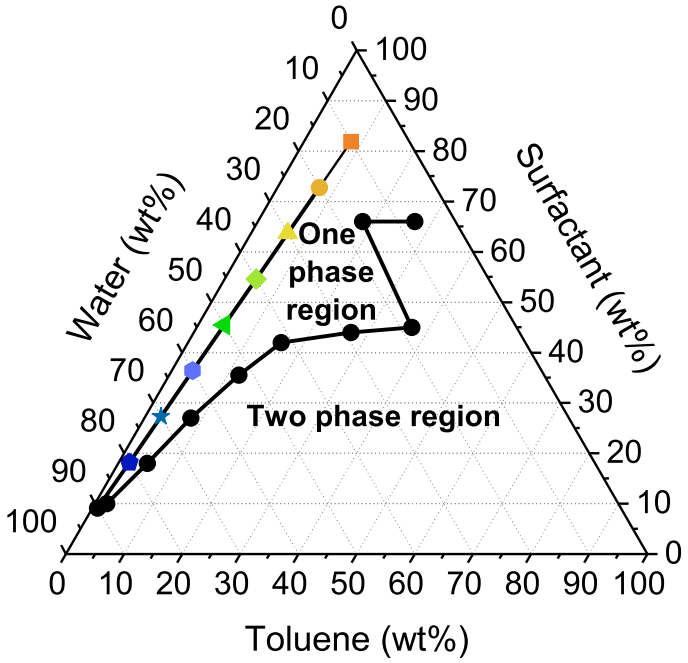


**Figure 3.1:** Ternary diagram of the polysorbate-20 stabilized microemulsions. The individual color symbols refer to the individual microemulsion compositions used in the fluorescent studies. The solid black line denotes the single phase region.

**Table 3.1:** Composition of microemulsion samples. Individual compositions are listed according to wt % water while the oil:surfactant ratio for all samples is held constant at 1:10.

| **Microemulsion sample** | **Toluene wt%** | **surfactant wt%** | **water wt%** |
|---|---|---|---|
| 10 % | 8.1 | 81.9 | 10 |
| 20 % | 7.2 | 72.8 | 20 |
| 30 % | 6.3 | 63.7 | 30 |
| 40 % | 5.4 | 54.6 | 40 |
| 50 % | 4.5 | 45.5 | 50 |
| 60 % | 3.6 | 36.4 | 60 |
| 70 % | 2.7 | 27.3 | 70 |
| 80 % | 1.8 | 18.2 | 80 |
| 90 % | 0.9 | 9.1 | 90 |

The concentration of c153 and r6g was maintained at 100 $\mu$M for all steady-state and time-resolved fluorescence experiments on single probe samples. The concentration of DPA was 10 $\mu$M. For Förster (fluorescence) resonance energy transfer (FRET) experiments, the concentration of c153 was kept at 100 $\mu$M while the concentration of r6g was varied from 0 to 100 $\mu$M with increments of 20 $\mu$M for each sample. For photoinduced electron transfer (PET) experiments, 15 $\mu$M of c153 and 75 $\mu$M of methyl viologen ($MV^{2+}$) were added to the microemulsion samples.

### 3.3.3 Steady-State Fluorescence Spectroscopy

Steady-state fluorescence measurements were carried out on a Cary Eclipse Fluorescence Spectrophotometer by Agilent. The emission spectra were collected at excitation wavelengths of 340 nm for laurdan, 400 nm for c153, 530 nm for r6g, and 390 nm for DPA.

The generalized polarization (GP) of laurdan is a steady-state fluorescence measurement that was first introduced by Parasassi *et al.* to quantitatively measure the phase transitions in model membranes.Parasassi et al. (1994) Specifically, a lower or more negative GP value is indicative of the increased presence of water in the interfacial environment in which laurdan is located. The GP function is defined as

$$GP = \frac{(I_B - I_R)}{(I_B + I_R)} \tag{3.1}$$

$I_B$ and $I_R$ are the fluorescence intensities at emission wavelengths of 440 nm and 490 nm, respectively, when the sample is excited at 340 nm. The partition coefficient (log P) value of c153 was calculated using ChemDraw Pro 20.

### 3.3.4 Time-Resolved Fluorescence Spectroscopy

Time-resolved fluorescence dynamics were measured on a home-built instrument using a time-correlated single-photon counting (TCSPC) module (PicoHarp 300,

PicoQuant). Briefly, an Nd:YAG pumped Ti:Sapphire oscillator yielding <100 fs laser pulses at 800 nm was used as the excitation light source. The repetition rate of 80 MHz was reduced to 13.33 MHz with an electro-optic modulator, and, for measurements of c153 and DPA, the output was focused into a $\beta$-barium borate (BBO) crystal for frequency doubling. The resulting 400 nm light was passed through a waveplate and a Glan-Taylor polarizer (excitation polarizer) to control the intensity and polarization of the excitation light before it was focused onto the sample cuvette. Fluorescence from the sample was passed through a second Glan-Taylor polarizer (emission polarizer) and bandpass emission filter (530/55 nm for c153 and 475/25nm for DPA) before it was focused on an avalanche photodiode. The data was acquired by PicoHarp 300 software. The same setup was used for the fluorescence anisotropy measurement of r6g by replacing the BBO crystal with a supercontinuum fiber (Newport FW800-0854), the output of which was filtered with a 530/55 nm bandpass filter to isolate the 530 nm excitation light. Fluorescence emission of r6g was filtered with a 572/28 nm bandpass filter. The instrumental response was measured with an aqueous solution of 100 $\mu$M DASPMILi et al. (2016) and was found to be ~40 ps FWHM. Fluorescence lifetime data was fit to a single exponential decay function for r6g while data from c153 and DPA required biexponential functions for adequate fits.

Anisotropy measurements were collected by acquiring fluorescence emission at parallel, magic angle (54.7°), and perpendicular polarizations relative to the excitation polarization. The isotropic intensity was calculated from parallel and perpendicular conditions according to

$$I_{iso}(t) = \frac{(I_{\parallel}(t) + 2I_{\perp}(t))}{3} \tag{3.2}$$

where $I_{\parallel}$ and $I_{\perp}$ are the parallel and perpendicular fluorescence intensities, respectively. Data were only accepted when the computed isotropic decay and the magic angle decay agreed within ±5%.Horng et al. (1997)

Anisotropy decays were calculated from re-convolution of the instrument response with the accepted parallel and perpendicular measurements and the following

equation

$$r(t) = \frac{(I_{\parallel}(t) - GI_{\perp}(t)}{(I_{\parallel} + 2GI_{\perp}(t))} \tag{3.3}$$

where the G-factor accounts for the polarization sensitivity of the detector and was measured to be ∼1.lak (2006a) Representative anisotropy measurements and decays can be found in the appendix as Figures A.1 and A.2, respectively.

The rotational anisotropy decays of microemulsion samples containing r6g were fit with monoexponential functions while samples containing c153 and DPA required biexponential functions for adequate fits:

$$r(t) = r(0)\left(a_1 e^{\frac{-t}{\tau_1}} + (1 - a_1)e^{\frac{-t}{\tau_2}}\right) \tag{3.4}$$

where $\tau_1$ and $\tau_2$ are the fast and slow relaxation times, respectively, and $a_1$ and $a_2 = (1 - a_1)$ are their corresponding amplitudes. Given the well-known multiexponential behavior for c153,Horng et al. (1997) only the weighted average of the rotational time ($\langle\tau\rangle$) for this probe was considered in our analysis:

$$\langle\tau\rangle = a_1\tau_1 + (1 - a_1)\tau_2 \tag{3.5}$$

All fittings were carried out with EasyTau 2.0 software (PicoQuant). These results are presented in full in Table A.1 .

## 3.4 Results and Discussion

### 3.4.1 Laurdan Hydration

Laurdan is an amphiphilic fluorescent probe with a well-studied sensitivity to the polarity of its environment. Parasassi et al. (1994) The emission spectra of laurdan in TBWT microemulsions of increasing water content is shown in Figure 3.2(a).

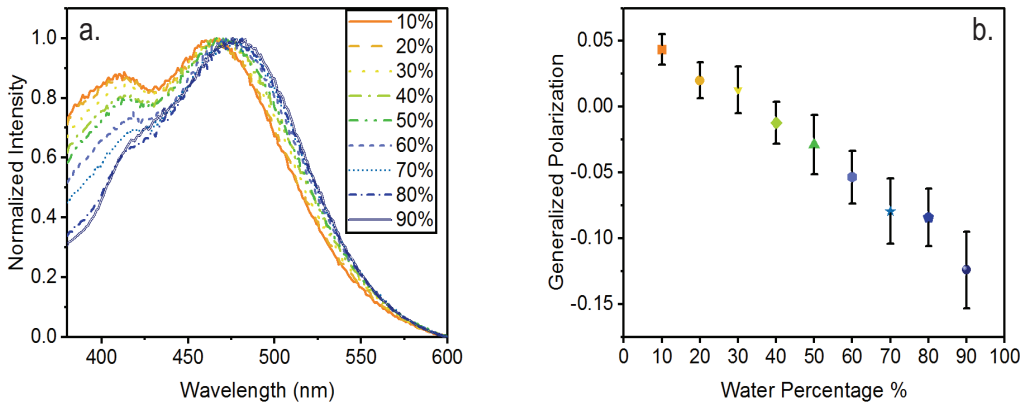


**Figure 3.2:** (a) Fluorescence emission spectra of laurdan in TBWT microemulsions of increasing water content as indicated in the legend. The samples were excited at 340 nm. As the water percentage increases, the intensity of the high energy peak decreases while the low energy peak shifts slightly to the red. (b) The GP values calculated from the spectra in (a). A linear change is observed as water penetrates into the surfactant layer. The colors of the individual traces and points in both plots match the compositions given in Figure 3.1.

A clear maximum is seen at ∼470 nm that red shifts with the addition of water. A shoulder at ∼420 nm is also apparent and loses significant intensity as the water content is increased. The position of these features is consistent with the spectra of laurdan in the individual components of the microemulsion system (see Figure A.7) and in agreement with a previous report of laurdan fluorescence emission in a different microemulsion system.Lissi et al. (2000)

In order to quantify the impact of this spectral evolution, the GP value for each composition was calculated and is plotted in Figure 3.2(b). For all laurdan fluorescence spectra, the excitation wavelength used was 340 nm and the GP emission was analyzed at 440 and 490 nm. These wavelengths were traditionally chosen for the study of phospholipid membranesParasassi et al. (1991) but have also been previously applied to the analysis of microemulsions.Lissi et al. (2000) The decreasing values of GP in Figure 3.2(b) show that the water is intercalating into the surfactant layer. While others have previously shown a more dramatic and exponential decrease in the GP with microemulsion hydration,Lissi et al. (2000) our results reveal a more modest, linear reduction. This difference arises from the broad compositional range over which the TBWT microemulsions maintain a bicontinuous phase. Overall, our laurdan results reflect a straightforward hydration of the surfactant domain as the microemulsion composition moves from surfactant-rich to water-rich.

Moving beyond the amphiphilic laurdan, we also examined the partitioning of ionic, polar and nonpolar chromophores within the microemulsion microenvironments. Specifically, c153 and r6g were chosen as the polarHorng et al. (1995) and ionic probes, respectively, due to their extensive use in fluorescence studies of complex fluid systems, including microemulsions. Adhikari et al. (2007); Bera et al. (2021); Chakrabarty et al. (2005) The steady-state fluorescence spectra of c153 in the 60% water microemulsions as well as in the individual non-aqueous components is shown in Figure 3.3(a). It is immediately apparent that the spectrum from c153 within the 60% water microemulsion is most similar to its emission in the surfactant components, especially butanol.

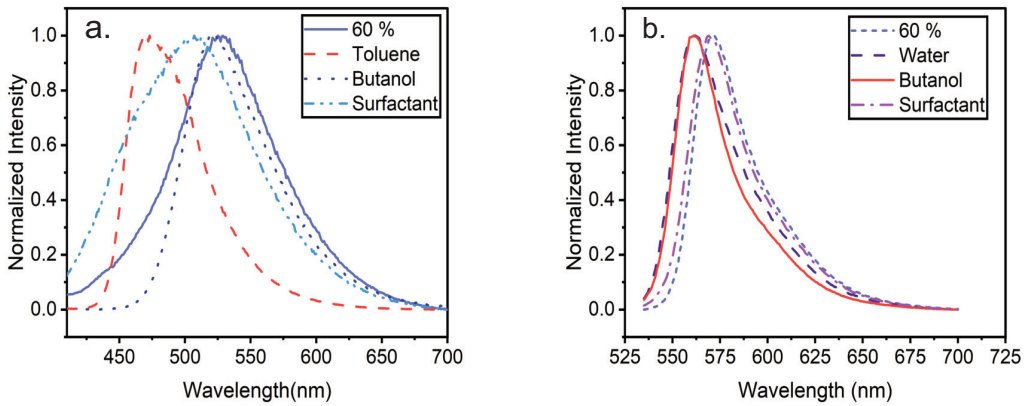


**Figure 3.3:** Fluorescence emission spectra of (a) c153 and (b) r6g in 60% water TWBT microemulsion and individual components. The surfactant is a mixture of butanol and Tween 20 as described in the text. The samples were excited at 400 nm for c153 and 530 nm for r6g. The emission from both probes in the microemulsion sample most closely resembles that observed from the surfactant.

This is not surprising given that c153 has a log$P$ (octanol: water partition coefficient) value of 3.51 suggesting moderate lipophilicity.Duncan et al. (2020) For context, a highly hydrophilic molecule would have a negative log$P$ value and a highly lipophilic molecule will have a positive log$P$ value, typically around 5.Wang et al. (2012) When the water content of the microemulsion is increased, a slight red shit of the c153 emission is observed (Figure A.3). The solvatochromatic behavior of c153 is well known with the red shift indicative of an increasingly polar environment.Jin et al. (2007); Horng et al. (1997); Reynolds et al. (1996) This is consistent with the laurdan results above showing water penetration into the surfactant layer for microemulsions with higher water loading.

The fluorescence emission spectra of r6g in Figure 3.3 (b). also indicate that this species associates with the surfactant layer. R6g is less lipophilic than c153 with a log $P$ value of 2.62,Wang et al. (2012) and the emission maxima of r6g in microemulsions did not show any variance with the composition change of the samples (Figure A.4).

### 3.4.2 Energy and Electron Transfer of Polar and Ionic Species

Given the presence of both c153 and r6g within the surfactant layer of the microemulsion and their known compatibility as FRET pair,Sahu et al. (2006); Ghatak et al. (2011) we collected a series of fluorescence spectra with both probes present to assess their relative distance. Figure 3.4 shows the fluorescence emission spectrum of the 90% water TWBT microemulsion sample containing 100 $\mu$M c153 with increasing amounts of r6g added. For all spectra, the c153 was excited at 400 nm. As the concentration of r6g increases in the sample, the c153 emission at ~530 nm decreases while emission from r6g at ~570 nm increases consistent with energy transfer from c153 to r6g.

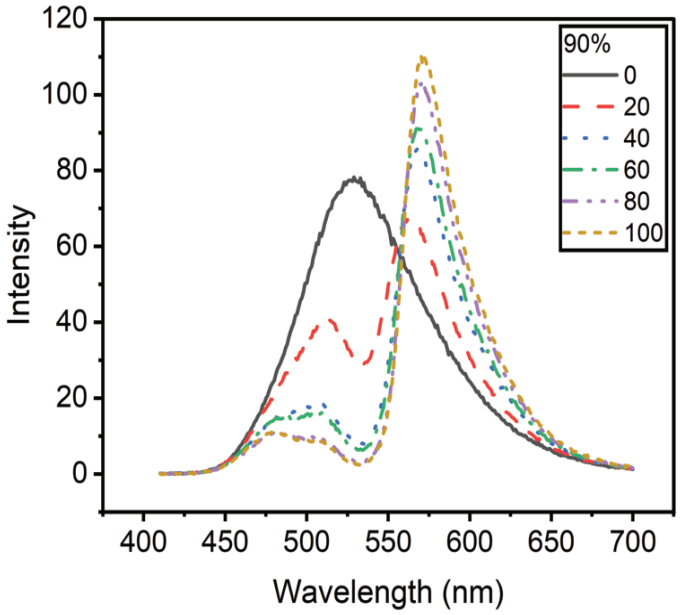


**Figure 3.4:** FRET of c153 and r6g in the 90% water TWBT microemulsion. The concentration of c153 in all samples is 100 $\mu$M and was excited at 400 nm. R6g concentrations are varied from 0 to 100 $\mu$M as indicated in the legend. As the concentration of r6g increases, the observed emission shifts from c153 to r6g indicating energy transfer.

Calculating the distance between the molecules from our measurements is difficult because the relative orientation of the molecules to each other is not known but is also *not* expected to be isotropically distributed given their association with the surfactant molecules. Previous work has shown that FRET is significantly impacted by the orientational arrangement of the molecules.Srinivas and Bagchi (2001)

In order to better assess how deep the c153 is buried within the surfactant layer, assuming that the ionic species are closer to the water domain, we conducted a complementary PET experiment. For this experiment, we replaced r6g with methyl viologen ($MV^{2+}$) as the ionic species as it is known to have a suitable reduction potential to facilitate energy transfer from c153.Porel et al. (2012) In comparison to rg6, $MV^{2+}$ is a smaller molecule which may suggest deeper penetration into the surfactant layer, but its +2 charge is expected to yield a higher water association. If electron transfer to $MV^{2+}$ occurs after c153 excitation, the emission intensity from c153 should decrease. As can be seen in Figure A.5 and A.6 , the fluorescence intensity of c153 does not change in the presence of $MV^{2+}$ indicating no PET. FRET efficiency is inversely proportional to the sixth power of the distance separation. In contrast, the dependence of PET on distance is exponential and primarily only effective at distances on the order of 10 Å. As such we find that the distance between the polar and ionic species is too far for electron transfer in our experiments but close enough for energy transfer.

### 3.4.3 Time-Resolved Anisotropy of C153 and R6g

After determining their localization, we next consider the rotational diffusion of r6g and c153 via dynamic fluorescence anisotropy measurements. Control experiments conducted on the probe molecules in neat solvents before carrying out measurements on microemulsion samples. Specifically, we measured the initial anisotropy and rotational time of c153 in butanol and r6g in water. The initial anisotropy and rotational time for c153 in butanol were measured to be 0.369 ± 0.006 and 234.1 ±

3.7 ps, respectively, while for r6g in water measurement values were 0.389 ± 0.005 and 251 ± 7.9 ps, respectively. These values are consistent with previous reports in the literature.Maroncelli and Fleming (1987); Horng et al. (1997); Gumy and Vauthey (1996); Philips et al. (1985) Figure 3.5 (a) and (b) shows the rotational times of c153 and r6g in the hydration series of TBWT microemulsions, respectively. It is immediately apparent that both probes display a similar trend consistent with their close proximity in the polar region of the surfactant layer. From 10-60% water loading, the rotational times of both probe species decrease as the increased hydration in the surfactant region reduces the local viscosity permitting faster rotational diffusion. Despite the continued increase in the hydration of the surfactant layer over the entire compositional range tested, however, the rotational rates of both probes show a minimum at 60% followed by increasingly hindered rotation at higher water percentages. As mentioned previously, the anisotropy decay of c153 was fitted with a biexponential function, whereas r6g was fitted with a monoexponential function. Previous work has shown that c153 exhibits multiexponential decays in its fluorescence lifetime in a wide range of neat solvents.Horng et al. (1997) As such, we do not associate the different decay components of c153 to heterogenous microenvironments and instead consider only the average rotational time, weighted according to the amplitudes of the individual components. It is worth mentioning that the initial anisotropy we measured in microemulsions is lower than that in neat solvents (butanol and water), which is consistent with previous reports in the literature for complex fluids.Funston et al. (2007); Carnero Ruiz et al. (2017); Adhikari et al. (2007); Bain et al. (2000); Oliveira et al. (2001); Blackburn et al. (1996) The similarity in the trends of rotational times observed for both of the probes supports the FRET results above that c153 and r6g reside in relatively close proximity in the surfactant microenvironment and sense similar local changes in the microemulsions. While the laurdan results described previously indicate that water is still penetrating in increasing amounts into the surfactant layer at these water percentages above 60%, this increase in water does not yield a more fluid environment.

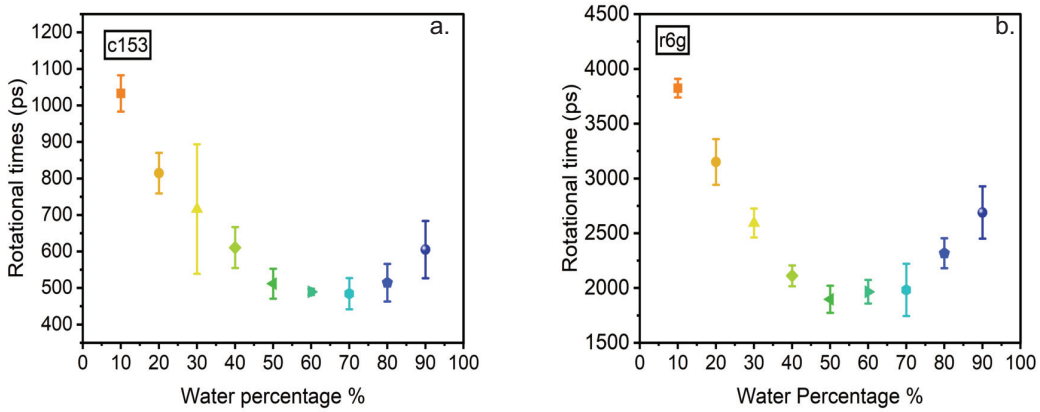


**Figure 3.5:** Rotational times of c153 (a) and r6g (b) in the TWBT microemulsions. The concentration of both of the probes was 100 $\mu$M. TWBT microemulsions with c153 were excited at 400 nm and emission was collected at 530 nm. R6g was excited at 530 nm and emission was collected at 572 nm. The decrease and subsequent increase of the rotational time correlates first to an increased surfactant layer fluidity due to water penetration and then to a stiffening and structural change in the microemulsions from bicontinuous to droplet.

Instead a stiffening of the surfactant layer is observed according to the rotational times of c153 and r6g. An important correlation to these results is that previous work has indicated that electron transfer in this 60% water microemulsions is most facile near this composition where we observe the most rapid rotational motion and hence the most fluid surfactant layer.Peng et al. (2020) In addition, the gradual transition from a bicontinuous structure to droplets in this microemulsion system has also been postulated to begin near this amount of water loading.Peng et al. (2020) Recent studies of these microemulsion samples by small angle neutron scattering show that the bending modulus, the energy needed to change the surfactant curvature at the interface, increases up to 60% water loading in the microemulsion samples and then decreases gradually as water loading increases beyond this point. The gradual decrease of bending modulus at higher water content was associated with the transition from bicontinuous to oil-in-water structure microemulsions.Imel et al. (2022) In this context, our results can then provide explanations for this observation as the increased water and resulting stiffening of the surfactant layer drives the larger structural change to droplets in this complex fluid.

### 3.4.4 Localization and Dynamics of Nonpolar Chromophore

The introduction of the nonpolar chromophore, DPA, reveals different behavior in contrast to the polar and ionic species. Figure 3.6 presents the fluorescence emission spectra of DPA in the surfactant mix, toluene, and TWBT microemulsions of varying water percentage. A red shoulder on the emission spectra is indicative of association with the surfactant environment but decreases with increased water loading until the DPA spectrum in the 90% water microemulsion matches that of DPA in toluene. Unlike the previous probes, this indicates a movement in the localization of the nonpolar species out of the surfactant layer as the microemulsion composition changes. This behavior of the nonpolar DPA is further confirmed by examining its rotational diffusion trends at 475 nm emission.

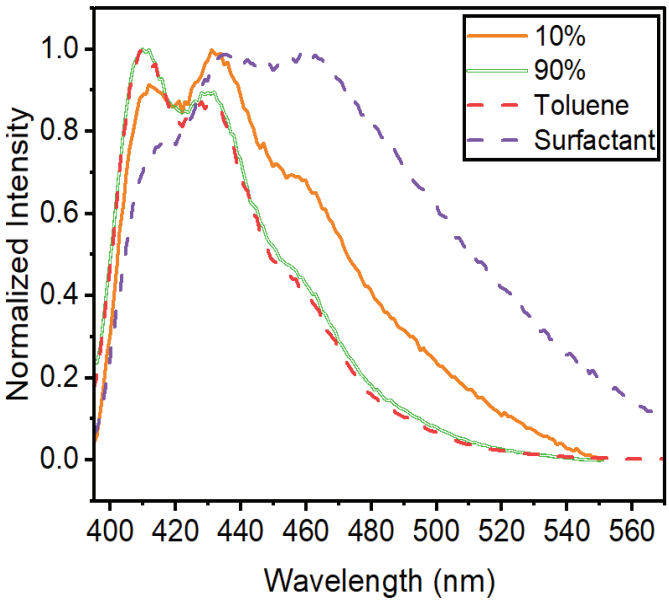


**Figure 3.6:** Fluorescence emission spectra of DPA in toluene, surfactant and TWBT microemulsions with 10 and 90% water. At lower water content, there is more association of the DPA with the surfactant layer. All samples contained 10 $\mu$M of DPA and were excited at 390 nm.

The anisotropy decay of DPA was fitted with a biexponential function. Unlike c153 and r6g, DPA does not show a minimum in rotational time at 60% water loading but instead a change in partitioning reflecting the microemulsion compositional change. Figure 3.7(a) and (b) shows both the rotational times and amplitudes for the fast and slow components of DPA in the microemulsion samples, respectively. The fast rotational component is constantly ∼600 ps for all microemulsion compositions, but the amplitude shows a maximum at 60% water loading consistent with a majority of the molecules partitioning into this environment when the surfactant layer is most fluid. The slow rotational component reveals a linear decrease as the water percentage increases in the system. The amplitude of the slow component mirrors that of the fast component with a minimum of the DPA molecules in this, more rigid, microenvironment at the 60% water composition. This increase in rotational time is expected to arise from a movement of this DPA microenvironment toward the oil domain as the water penetration in the surfactant layer increases. While the steady state emission spectra of DPA in 90% microemulsion and toluene resembles each other, the rotational time of DPA in the all of the microemulsion samples is much slower than in neat solvents.Ben-Amotz and Scott (1987)

## 3.5 Conclusions

Microemulsions are complex fluids, and their ability to solvate a diverse range of small molecules in different domains is important to their many applications. In this series of fluorescence measurements, we find that all small molecule probes studied, despite their structural differences, show partitioning into the surfactant layer of the nonionic TWBT microemulsion system. In fact, the ionic and polar species are close enough to permit energy transfer between them. As the water content increases beyond 60%, the rotational dynamics of c153 and r6g report on a stiffening of the surfactant layer that correlates with a larger structural change in the microemulsion from bicontinous to droplets.

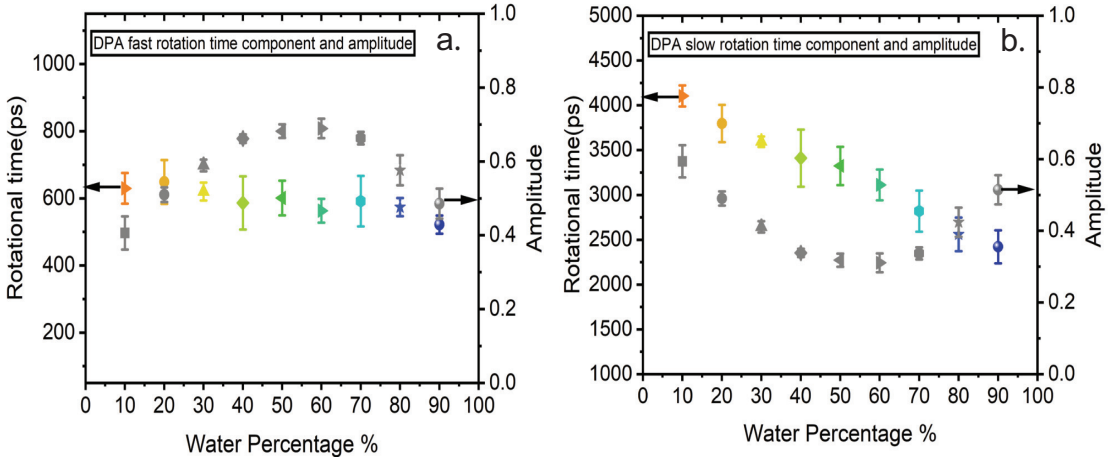


**Figure 3.7:** DPA fluorescence anisotropy in in TWBT microemulsions. (a) Fast rotational time components and amplitudes as a function of water percentage. The amplitude increases as water increase until 60% and decreases with further increase of water while the rotational times remains relatively constant. (b) Slow rotational time components and amplitudes. The time component decreases with the increase in water content while the amplitude decreases until 60% water loading and then increases with water addition. Overall, DPA shows changes in partitioning as a function water content in the microemulsion.

In contrast, the nonpolar DPA associates more with the surfactant tails and oil domain as water increasingly penetrates the surfactant layer (Figure 3.8). Overall, our results support the hypothesis that the microemulsion surfactant layer can mediate the partitioning of a range of different small molecules and act overall as a tunable environment.

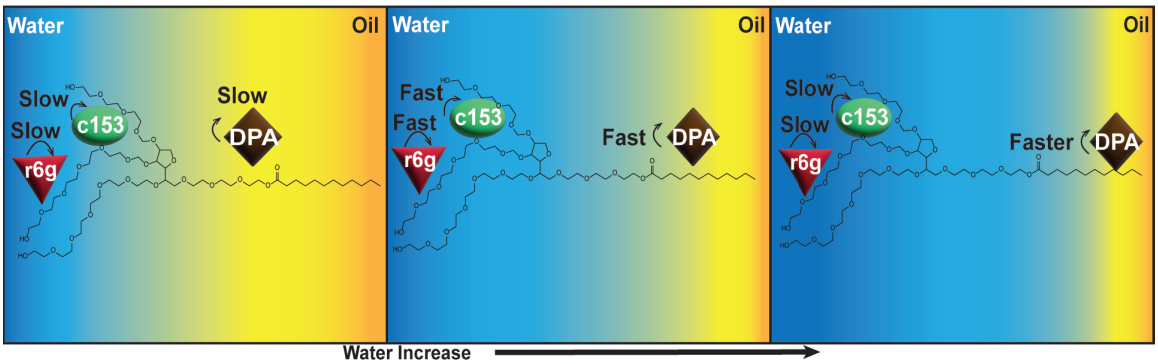


**Figure 3.8:** A graphical representation of microemulsion's microenvironment, showing possible sorting of different probe molecules around the Tween 20 structure at different water percentage.

# Chapter 4

# Exploring the Heterogeneity in ChCl:Phenol Deep Eutectic Solvents by Fluorescence Techniques

## 4.1 Introduction

Deep eutectic solvents (DESs) are tunable complex fluids that have numerous applications in industrial and scientific fields including, metal processing and metallurgy Abbott et al. (2007), batteriesSöldner et al. (2019), solar cells Pal et al. (2014), gas separation Kadyan et al. (2016); García et al. (2015), nanomaterial synthesis Wagle et al. (2014), pharmaceuticals, Mano et al. (2017) biocatalysis, Durand et al. (2013) biomaterial manufacturing, Loow et al. (2018) and genomics Domínguez de María and Maugeri (2011). DESs are eutectic binary mixtures containing a hydrogen bond acceptor (HBA) and a hydrogen bond donor (HBD) species whose melting temperature is lower than that of the individual constituents. These fluid systems were first formulated by Abbot et al.Abbott et al. (2003), when powdered choline chloride and crystalline urea were mixed at 1:2 mole ratio, it was observed that the mixture turned liquid at room temperature. The decrease of the mixture's melting point is a result of the formation of hydrogen bonds between the halide ions and hydrogen-donor moieties. Since that discovery, many DESs of various binary mixtures of hydrogen bond acceptor (HBA) and HBD have been formulated and studied till date and, many more ($10^8$) binary mixtures have been theorized. Hansen et al. (2021)

DESs are often acknowledged as a class of ionic liquids (IL) Smith et al. (2014), another complex fluid made of distinct ions, because of their similar physical properties including thermal stability, low volatility, non-flammability, low vapor pressure, and tunability. Hansen et al. (2021); Smith et al. (2014) However, DESs and ILs have many important differences. ILs are made from limited types of discrete anions and cations and are liquid at $< 100^oC$ temperature, whereas DESs are made from various eutectic mixtures of HBA and HBD species and are liquid at room temperature. Smith et al. (2014) DESs are easy and economically more feasible to synthesize compared to ILs. Like ILs though, DESs have the potential to become an alternative to aqueous electrolytes. Subba et al. (2020); Dhingra et al. (2019);

Wang et al. (2012) Current DESs are however limited by high viscosity which is not favorable for electrolyte application. Thus, fundamental understanding of the molecular arrangement of DESs components is required for tailoring appropriate DESs with lower viscosity and higher solubility properties.

There are many experimental techniques available to characterize DESs including, nuclear magnetic resonance, fourier-transform infrared spectroscopy, broadband dielectric spectroscopy, neutron scattering, dynamic light scattering, and fluorescence spectroscopy.Hansen et al. (2021); Pandey et al. (2013); Das and Biswas (2015); Pandey et al. (2017); Sakuragi et al. (2018); Söldner et al. (2019) In this research work, fluorescence techniques including steady-state fluorescence and time-resolved fluorescence anisotropy were employed to characterize DESs made of choline chloride and phenol. This sample was chosen because recently it has been seen that electrical conductivity of choline chloride:phenol DESs is comparable to the conductivity of ionic liquids. Generally ionic liquids have higher electrical conductivity than DESs. To the best of our knowledge, the DES samples that are studied here have not been previously characterized using fluorescence techniques.

Fluorescence techniques have been employed to investigate various properties of DESs including solvation dynamics, rotational diffusion, translational diffusion, polarity, spatial, and temporal heterogeneity of DESs. Subba et al. (2020); Hossain et al. (2020); Kadyan et al. (2019); Turner and Kim (2018); Hossain et al. (2019); Pandey et al. (2017); Guchhait et al. (2010); Das et al. (2015) Here in this work, we employed two dipolar probes, c153 and 4-aminophthalimide (4AP), and a nonpolar probe DPA, to investigate the microenvironments of the ChCl:Phenol DESs by steady-state and time-resolved fluorescence techniques. The inherent properties that these individual probes possess include the environment sensitivity of c153, affinity for hydrogen bonding of 4AP and neutral interaction of DPA. Steady-state fluorescence studies were employed to study the polarity and spatial heterogeneity of the microenvironments of DESs. Time-resolved fluorescence anisotropy was used to assess the mobility of the probes in these complex fluid systems.

## 4.2 Materials and Methods

### 4.2.1 Chemicals

Choline chloride, anhydrous phenol, and DPA were purchased from Fisher Scientific. 4AP was purchased from Thermo Fisher Scientific, and c153 was purchased from Exciton. All solvents and small molecule probes were used as received.

### 4.2.2 Deep Eutectic Solvent Preparation

Choline chloride and phenol were dried for 48 hrs prior to sample preparation. Appropriate amounts of solid choline chloride and phenol were added in a vial. The processes of weighing and mixing the components were carried out under a gentle stream of nitrogen gas in a glove box. After adding the solids in a vial, the mixture was mixed using a stir bar in presence of gentle heat around $55^{o}$C by placing the vial on top of a hot plate. The mixture was stirred until a clear homogeneous liquid appearance was achieved. After the samples were cooled down to room temperature probe molecules were added to the samples for fluorescence experiments. Table 4.1 shows the molar ratio of the choline chloride and phenol in each samples that was tested in this study. The number in the sample name reflects the mole ratio of HBD (phenol) to choline chloride in each DESs. The higher number (6) indicates the presence of higher phenol content (6:1) in the samples compared with lower number labels. All the samples retained liquid form throughout the experiments and while stored at room temperature.

### 4.2.3 Steady-State Fluorescence Spectroscopy

Steady-state fluorescence measurements were carried out on a Cary Eclipse Fluorescence Spectrophotometer by Agilent. Samples with c153 were excited at 365 nm, 390 nm, 400 nm and 420 nm. 4AP dissolved samples were excited at 365 nm, 390 nm, 400 nm and 420 nm and samples containing DPA were excited at 390 nm.

**Table 4.1:** Composition of DES samples, in each sample HBD was varied

| **Sample Name** | **ChCl:Phenol mole ratio** |
|---|---|
| DES_2 | 1:2 |
| DES_3 | 1:3 |
| DES_4 | 1:4 |
| DES_6 | 1:6 |

### 4.2.4 Time-Resolved Fluorescence Spectroscopy

The home-built instrument that was described in chapter 3 was used to collect the time-resolved fluorescence measurements in this work. Briefly, The laser pulse of $<$ 100 fs at 800 nm from Nd:YAG pumped Ti:Sapphire oscillator (Mai Tai) was passed through an electro-optic modulator to modulate the repetition rate of the light to 13.33 MHz from 80 MHz. The modulated light was focused into a $\beta$-barium borate (BBO) crystal to generate 400 nm light. The 400 nm light was used as the fundamental light for the instrument. In the instrument, the 400 nm light passed through a waveplate and a Glan-Taylor polarizer (excitation polarizer) to control the intensity and select the polarization of the excitation light. The selected polarized light (vertical polarization) was focused onto the sample cuvette. The fluorescence from the sample was collected at a $90^o$ angle with a series of lenses. The fluorescence was then passed through a second Glan-Taylor polarizer (emission polarizer) to select the parallel or perpendicular polarized fluorescence. Selected polarized fluorescence was passed through the bandpass emission filters to filter out the fluorescence from fundamental light. Subsequently, the fluorescence was focused on an avalanche photodiode. To isolate fluorescence of c153 and 4AP from the respected samples, a 530/55 nm and a 525/20 nm bandpass filters, respectively were used. Fluorescence of DPA was filtered by 475/25 nm bandpass. The avalanche photodiode sent the signal to the time-correlated single photon counting module (PicoHarp 300, PicoQuant). Using the Picoharp 300 software the data was acquired. The fitting was done using Easy Tau 2 software. The instrumental response was measured with an aqueous solution of 100 $\mu$M DASPMI Li et al. (2016) and was found to be $\sim$40 ps FWHM.

Time-resolved fluorescence emission data were checked for quality by comparing the calculated isotopic intensity decay with the magic angle intensity decay (fluorescence collected at a 54.7° with respect to the excitation polarization). When these decays agreed within $\pm$5%, Horng et al. (1997) the parallel and perpendicular data were considered for anisotropy calculations. The isotropic intensity was calculated by

computing the parallel intensity, $I_{\parallel}$, and perpendicular intensity, $I_{\perp}$, in the equation 4.1.

$$I_{iso}(t) = \frac{(I_{\parallel}(t) + 2I_{\perp}(t))}{3} \tag{4.1}$$

Anisotropy decays, $r(t)$, were calculated by computing the parallel and perpendicular intensity in the following equation,

$$r(t) = \frac{(I_{\parallel}(t) - GI_{\perp}(t)}{(I_{\parallel}(t) + 2GI_{\perp}(t))} \tag{4.2}$$

The G factor is the factor that corresponds to the polarization bias of the detector and was ∼1. lak (2006a) The anisotropy decays were fitted with the following equation by re-convolution of the instrument response.

$$r(t) = r(0)(a_1 e^{\frac{-t}{\tau}}) \tag{4.3}$$

The anisotropy decays of c153 were fitted with biexponential function whereas the anisotropy decays of 4AP and DPA required monoexponential fits. All the fitting were done by employing Easy Tau 2 (PicoQuant) software.

## 4.3 Results and Discussions

### 4.3.1 Steady-State Fluorescence

Figure 4.1 shows representative fluorescence emission spectra of c153, DPA, and 4AP dissolved in choline chloride:phenol DESs at room temperature. These probes are commonly used in the fluorescence studies of DES. Hossain and Samanta (2018); Hossain et al. (2019); Das and Biswas (2015); Subba et al. (2020) The non-polar probe DPA showed very similar emission behavior in the DESs across all the composition. The phenol content change in its surrounding environment did not influence any emission behavior.

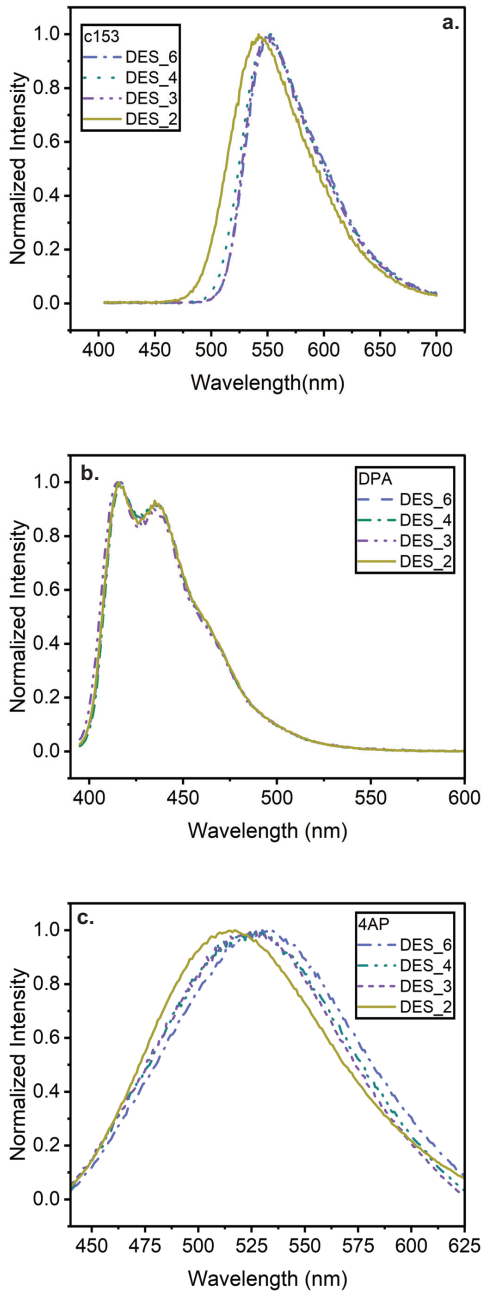


**Figure 4.1:** (a) Emission spectra of c153 in choline chloride:phenol DESs. The peak emission shifts to red with the increase of phenol content, (b) Fluorescence of DPA in DESs showing no change in their fluorescence spectra with different mole ratios of HBD, (c) emission spectra of 4AP showing continuous with increasing phenol composition in the system.

In chapter 3, DPA showed movement in microemulsions with the increase in water loading. Here, unlike in microemulsions, DPA did not show any sign of movement in the DESs. The emission spectra of c153 and 4AP display clear solvatochromic shifts in the DESs. Hossain et al. (2019). Figure 4.1(a) shows a 9 nm red shift of emission maxima of c153 with the increase of phenol from DES_2 to DES_3. The further increase of phenol in DES_3 to DES_6, however, did not result in an additional red shift of the c153 emission maxima. Previous studies of c153 have shown that this probe's emission spectra shift in response to the polarity of its environment suggesting that the polarity of c153's local environment in DES_3 to DES_6 is not changing. The dipolar probe 4AP did show a red shift of its emission maxima with the increase of phenol content across all the compositions of the DESs (Figure 4.1). 4AP can sense polarity change in its local environment and is also prone to interact with hydrogen bonds. Hossain and Samanta (2018) The emission spectra of 4AP in Figure 4.1 (c) shows a red shift with the increase of phenol content in the DES indicating its interaction with the hydrogen bond network in its local environment.

### 4.3.2 Spatial Heterogeneity

The formation of DES systems through hydrogen bonding between HBAs and HBDs can give rise to heterogeneity in the system. The study of spatial heterogeneity in DESs employing excitation-dependent fluorescence technique is common in the literature. Biswas and coworkers have studied this phenomenon in various DESs including ChCl:urea Das and Biswas (2015), glucose:urea:water Tarif et al. (2019), acetamide:calcium nitrate Subba et al. (2020), acetamide:urea Das et al. (2015), and acetamide:polyethylene glycol Reuter et al. (2021). Samanta and coworkers have also studied spatial heterogeneity in alcohol-based DESs including ChCl:1,2-ethanediol, ChCl:1,3 propanediol, ChCl:1,4-butanediol, and ChCl:ethylene glycol Hossain and Samanta (2018, 2017).

As shown in Figure 4.2 if a dipolar molecule is surrounded by nonidentical microenvironments, probing that molecule at different excitation wavelengths will show a shift in the corresponding emission maxima which will reflect the microheterogeneity of the medium. We investigated the excitation-dependent fluorescence of c153 and 4AP in our DES samples as shown in Figure 4.3. The results of c153 show no excitation-dependent emission behavior, meaning there is no shift in emission maxima at the different excitation wavelengths. However, we do see the emission maxima of 4AP shift when the probe is excited at different wavelengths. The maximum shift of the 4AP emission peak is seen for DES_3, where the shift is about 20 nm. When 4AP in DES_3 is excited at 375 nm the emission peak is observed at 516 nm but when excited at 420 nm the emission peak is observed at 536 nm. In the literature, it is not common to see excitation-dependent fluorescence in 4AP but not in c153. Hossain and Samanta (2017, 2018) Given the different behavior of c153 and 4AP, we interpret the excitation-dependent behavior of 4AP as likely arising from its interaction with the hydrogen bond network, which c153 is less sensitive to, than spatial heterogeneity. To confirm the lack of 4AP population in two different local environments, we can look further at our time-resolved fluorescence data. The spatial heterogeneity can be investigated by better fluorescence techniques, for example, fluorescence correlation spectroscopy (FCS). Subba et al. (2020); Hossain et al. (2019)

### 4.3.3 Time-Resolved Anisotropy

After observing the steady-state fluorescence in these DESs, we evaluate the influence of local environment on the rotation of the probe molecules by measuring the time-resolved fluorescence anisotropy. Figure 4.4 shows the rotational times derived from anisotropy measurements of probes c153, 4AP, and DPA in the DES samples.

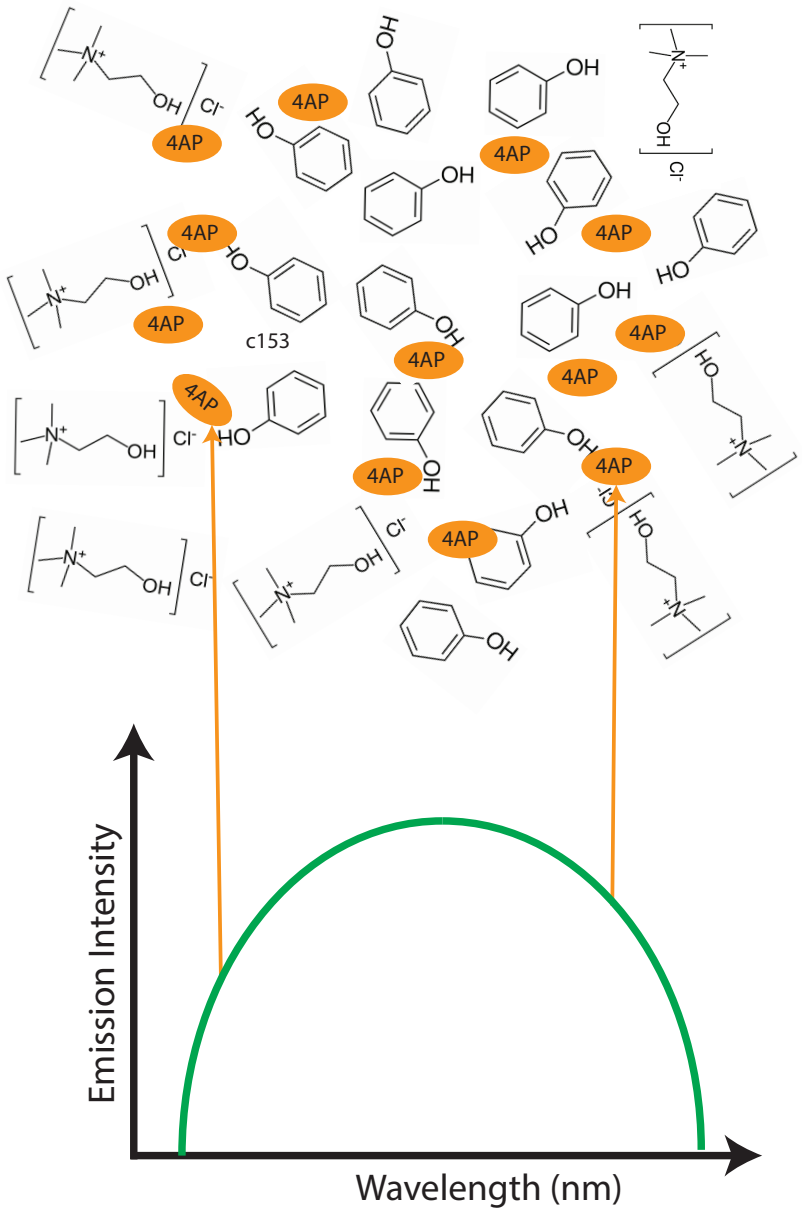


**Figure 4.2:** A schematic representation of possible sorting of 4AP in the ChCl:Phenol DES. The fluorescence spectra of 4AP in DES shows how emission intensity at an wavelength correspond to the population of 4AP situated in the DES. The 2 4AP molecules that have lines drawn from them appear to be in the same local environment.

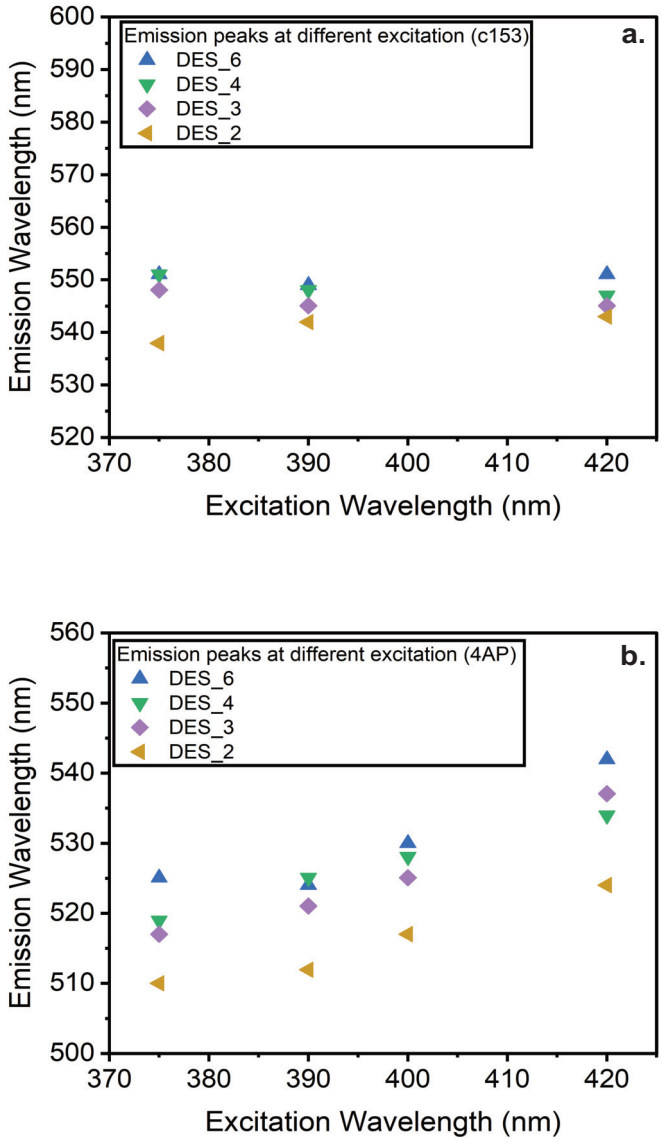


**Figure 4.3:** The excitation-dependent emission of (a)c153 and (b)4AP in DESs, c153 shows no difference in their peak emissions at different excitations. However, distinct changes in the peak emission of 4AP in DESs are seen at different excitation wavelengths.

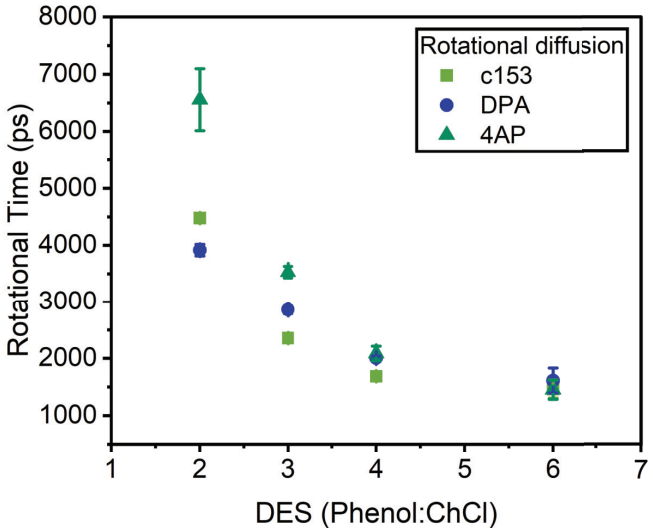


**Figure 4.4:** Rotational times of (a)c153, (b)DPA, and (c)4AP in Phenol:ChCl DESs. The rotational times of all the probes decreases with the increase of phenol in the system.

Despite being distinctly different from each other, the probes show a similar trend of rotational rates. We observe a decrease in rotational times with an increase in the molar ratio of phenol:ChCl for all the probes. The decrease in rotational time indicates that the probe is rotating more freely in the solvent environment, feeling less hindrance. This trend follows the viscosity trend of these same DESs studied by Guo *et al.* Guo et al. (2013) where they observed the decrease of viscosity with increasing phenol content. Our previous interpretation of the steady-state fluorescence data suggested that the excitation-dependence of 4AP was not due to the probe experiencing multiple local environments which is further supported our time-resolved data here as the 4AP emission decay was fit with a single exponential decay. If 4AP was distributed at different sites in the DES, the fluorescence would be expected to decay in multi-exponential form with different dynamics arising from the different populations. It is also possible that we were not able to probe 4AP that were sorted in the different local environments as time-resolved fluorescence signals were isolated using a single, narrow bandpass, emission filter.

The rotational rate of the probe molecule is directly influenced by the local viscosity. If we see the rotational time of c153, DPA, and 4AP in DES_6 we observe that they are reporting a similar rotational time of $\sim$ 1700 ps. Although the size of 4AP is the smallest of the probes studied, it rotates at similar rate as c153 and DPA suggesting its rate is hindered. As it is the only one of the three molecules expected to significantly interact with the hydrogen bond network, we postulate that this interaction is reducing its rotation. To evaluate this hypothesis, we calculate the theoretical time of 4AP and c153 in DESs using the Stoke-Einstein-Debye (SED) hydrodynamic equation Fleming and Fleming (1986),

$$\tau_{rot} = \frac{\eta V f C}{K_B T} \tag{4.4}$$

Here, $\tau_{rot}$ is the rotational time, $V$ is the van der Waals volume of the solute, $f$ is the shape factor of the solute, $C$ is the boundary case (either stick or slip), $K_B$

is the Boltzmann constant and $T$ is the temperature. For our analysis, we calculate the theoretical rotational times of these probes in stick and slip boundary conditions. Briefly, the slip and stick boundary conditions indicate the extent of solute-solvent coupling. The values of hydrodynamic slip ($C_{slip}$) and shape factor ($f$) for c153 were 0.24 and 1.71, respectively. Hydrodynamic slip and shape factor for 4AP were 0.11 and 1.60, respectively. The values of $V$, $C$, and $f$ for c153 and 4AP were taken from the literature Hossain and Samanta (2018). Figure 4.5 compares the rotational times extracted from experimental data with the calculated stick and slip rotational time as a function of the DES composition. Figure 4.5 (a) shows the experimental rotational times of c153 in DESs lie in between the slip and stick model indicating moderate interaction of c153 with the solvent. The semi slip and stick interaction of c153 with solvents is well known in the literature. Hossain and Samanta (2018, 2017) On the other hand, the experimental rotational times of 4AP(Figure 4.5 (b)), are higher than the rotational times from the stick model. The deviation of the experimental rotational time of 4AP from the stick model time decreases with the increase of the phenol content in the DESs. This shows the weakening of the hydrogen bond interaction with 4AP. In literature, it has been shown that the strength of the hydrogen bond between HBA and HBD relies on the substitution group of the HBD. Zhu et al. (2017) The electron-withdrawing substituting group strengthens the hydrogen bond, and the electron-donating substitution group weakens the hydrogen bond between HBA and HBD. Zhu et al. (2017); Stefanovic et al. (2017) A weak hydrogen bond network corresponds to a lower viscosity of DES. In our sample, phenol has the electron-donating substitution group and with the increase of phenol concentration in the DES decreases the strength of the hydrogen bond, hence lowering the viscosity. Guo et al. (2013) This correlates with the trend we see in the decrease of deviation of the experimental rotational time of 4AP from the stick model rotational times of 4AP.

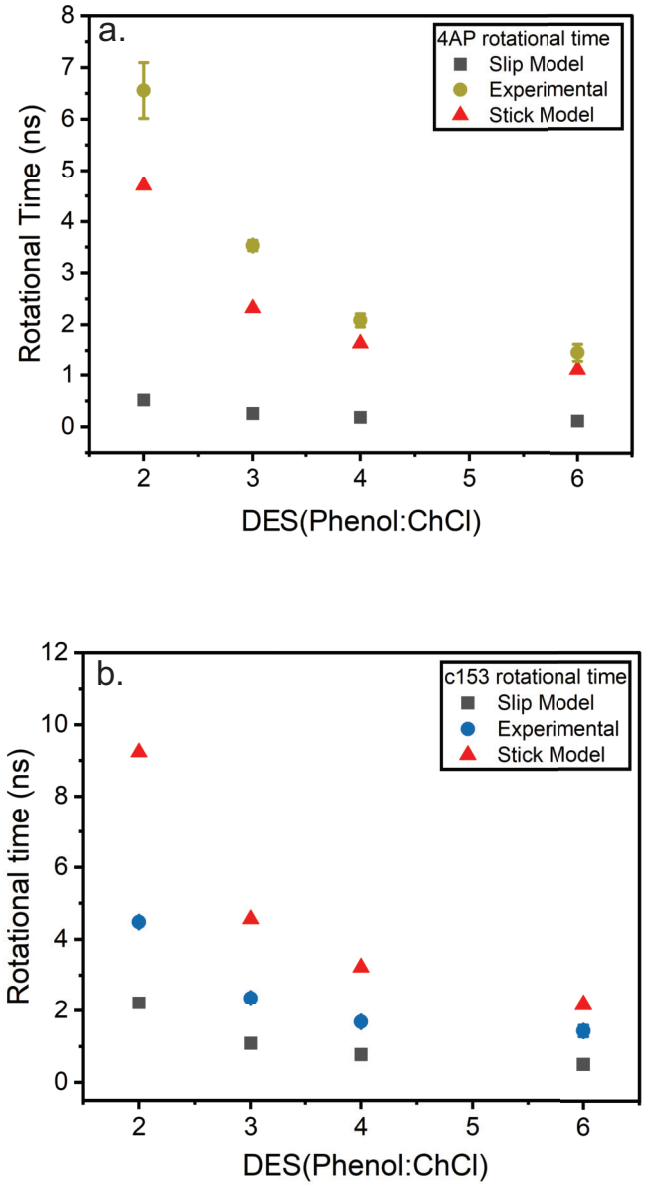


**Figure 4.5:** The experimental rotational times of c153 and 4AP in the DESs are plotted with the theoretical rotational times calculated from slip and stick hydrodynamic model for the same probe across all the composition of DESs.

## 4.4 Conclusions

DESs are complex and versatile solvent systems that are capable of replacing volatile organic solvents and aqueous electrolytes because of their tunable properties, ease of formulation, and biodegradability. Here, we have studied a series of eutectic mixtures of choline chloride and phenol by employing multiple fluorescence techniques. While excitation-dependent fluorescence emission was observed for 4AP, the presence of spatial heterogeneity was not supported by steady-state c153 measurements or time-resolved studies. Instead, the 4AP steady-state results may arise from different hydrogen-bonding interactions which are strong in this system as characterized by its superstick behavior. Only small differences were noted in the behaviors of the probes for different DES compositions, but the most notable was the reduction of hydrogen-bonding interaction of 4AP with the relative increase of the phenol concentration. Future studies to investigate how this trend extends to systems with even higher phenol content may be warranted.

# Chapter 5

# The Adsorption Dynamics of Nonionic Surfactants at Charged Surfaces probed by Second Harmonic Generation Spectroscopy

## 5.1 Introduction

Surfactants are amphiphilic molecules, soluble in both polar and non polar solvents by leveraging their hydrophilic and hydrophobic parts. These molecules have numerous industrial applications as surface-active agents, including detergents, microemulsions, oil recovery, drug delivery systems, and cosmetics.Israelachvili (1994); McClements and Rao (2011); Sjöblom et al. (1996); Soloveichik (2015b) Surfactants have the unique properties of reducing surface tension and interfacial tension between phases. Prince (1967) Another important property of surfactants is their adsorption at solid surfaces.Wang et al. (2000) Surfactants are often used to modify the electrode surface in electrochemical cells to improve reaction rates.Vittal et al. (2006) A recent study on a microemulsion system's potential application as an electrolyte revealed that the surfactant layer in the microemulsion facilitates facile electron transfer rates at the electrode.Peng et al. (2020)

For efficient electron transfer at the electrode, the electroactive agent must donate/accept electrons at the surface of the electrode and transport itself into the bulk. If surfactants at the electrode are adsorbed in a way that impacts the movement of the electroactive species, the rate of electron transfer at the electrode will be altered. To screen for this behavior, the adsorption of small molecules onto charged surfaces in the presence of different surfactants can be characterized. If the surfactants hamper the mass transport it would be beneficial to select a surfactant that would have low adsorption affinity towards a charged surface or vice versa for cases where the surfactant does facilitate the mass transport. The goal of this project is to use second harmonic generation spectroscopy to characterize the surface adsorption of surfactants and the role of surfactant on the adsorption of small molecules at the charged surface to aid the selection of surfactants for future application in electrolytes.

Second harmonic generation spectroscopy is surface-specific that can report on the events taking place at the surface of solid particles buried in a bulk material, as such, this technique is often used for measuring the adsorption isotherms of small molecules

on charged surfaces. SHG spectroscopy has previously been utilized to study the dynamics of dye adsorption, polymer adsorption, micro-pollutant adsorption, and thiol adsorption.Wang et al. (2000); Eisenthal (2006); Jen et al. (2009); Jen and Dai (2006) One of the criteria to increase SHG signals from molecules adsorbed at a surface dispersed in solution is that molecules have a resonant excited state at the SHG frequency. Our subject surfactant molecules do not meet this criteria. However, Wang *et al.*Wang et al. (2000) developed a method in which the adsorption of nonresonant molecules at a surface is studied by observing the displacement of adsorbed resonant molecules. SHG signal from the resonant molecules adsorbed at the surface will decay when a nonresonant molecule replaces them. The SHG decay of the resonant molecule can be fit with a competitive adsorption model to quantify the parameters of adsorption of the nonresonant molecule, in our case the surfactant molecules. We will be utilizing this method to study the adsorption isotherm of two nonionic surfactant molecules, Tween 20 and BrijO20, at the negatively charged surface (sulfate-functionalized polystyrene beads).

## 5.2 Experimental Section

### 5.2.1 Chemicals

Malachite green (MG) dye and the sulfate functionalized polystyrene beads (PS) were purchased from Thermo Fisher Scientific. Polysorbate 20 (Tween 20), and polyoxyethylene (20) oleyl ether (BrijO20) were purchased from Fisher Scientific. MilliQ deionized water (Millipore Sigma, Burlington, MA) was used to prepare samples. All the chemicals were used as received.

### 5.2.2 Instrumentation

The home-built SHG spectroscopy setup discussed in chapter 2 (Figure 2.4) was used to collect the data shown in this chapter. Briefly, the 800 nm light with a pulse width

of <100 fs at the repetition rate of 80 MHz from an Nd:YAG pumped Ti:Sapphire oscillator was used as the fundamental light for SHG. The light passes through a power attenuator consisting of a half- waveplate and a polarizer. Subsequently, it is passed through a 475 nm long pass filter before focusing the light onto the sample cuvette to ensure that the fundamental light is free of second harmonics which may be generated from the optics. In order to stir the sample between measurements, a magnetic stirrer was placed under the cuvette holder. SHG scattering from the sample was collected by a series of lenses (collection lenses) and passed through a 725 nm shortpass fiter (to filter out the fundamental 800 nm light from the SHG) before it was focused onto an optical fiber. The other end of the optical fiber was mounted on a filter cube where a 400/10 nm bandpass filter was placed. The filter cube was mounted on a Hamamatsu PMT counter head which collected the SHG signal. Using homebuilt LabView software, the data were acquired from the PMT and analyzed using MATLAB codes.

### 5.2.3 Sample Preparation

The samples were prepared by diluting a stock solution of PS beads in water to maintain a particle density of $10^8$ beads per ml. The solution pH was maintained at 4.1 because the MG dye exists in its cationic form at pH 4.1.Wang et al. (2000) The cationic form of the dye will ensure proper adsorption to the negatively charged surface. The $C_{2v}$ symmetry of MG exist at the cationic form, the SH light is resonance with the $C_2$ rotation axis. Eckenrode et al. (2005) Tween 20 and BrijO20 stock solutions were made with pH 4.1 water.

### 5.2.4 Adsorption Isotherm and Competitive Adsorption Isotherm Experiments

As mentioned earlier we will be utilizing the competitive adsorption isotherm method to study the adsorption isotherm of the surfactants. Before we can use this method,

we need to study the adsorption isotherm of the resonant molecules at the same negatively charged polystyrene beads because fitting parameters of the competitive isotherm model require the input of the adsorption parameters of the resonant molecules. Briefly, the adsorption isotherm experiment started with a sample containing $10^8$ polystyrene beads per ml dispersed in the aqueous solution of pH 4.1. An appropriate aliquot of MG stock solution was gradually added to the sample between each measurement. The sample was stirred for 30 s using a magnetic stirrer after the addition of MG solution to ensure proper mixing. After each addition of MG, the SHG signal from the adsorbed MG molecules in the sample was collected for 3 s at an integration time of 250 ms.

In competitive adsorption isotherm experiments, the starting sample contained $10^8$ polystyrene beads per ml dispersed in a 10 $\mu$M MG dye solution at pH 4.1. A small aliquot of surfactant stock solution was added to gradually increase the surfactant concentration in the sample. The amount of gradual increase varied between different surfactants. For the Tween 20 competitive isotherm experiment, the gradual increase of surfactant was kept at 0.25 $\mu$M. For BrijO20 the initial gradual increase was by 0.5 $\mu$M and after reaching the global concentration of 4 $\mu$M, the gradual addition was kept at 2 $\mu$M. The addition of surfactant to the sample was carried out until the SHG signal reached a plateau. Wang et al. (2000); Jen et al. (2009); Eisenthal (2006); Eckenrode and Dai (2004); Eckenrode et al. (2005); Cole et al. (2019)

Figure 5.1 shows a graphical representation of differences between two types of isotherm experiments. Figure 5.1 (a) represents an adsorption isotherm experiment where SHG intensity is plotted as a function of MG dye concentration. SHG signal increases with the increase of MG dye concentration in the solution as the MG dye get adsorbed at the bead surface. The signal reaches a plateau when the bead surface sites are filled by the MG dye molecules. By fitting this data with the modified Langmuir adsorption model, the adsorption energy and number of active sites can be extracted. Wang et al. (2000)

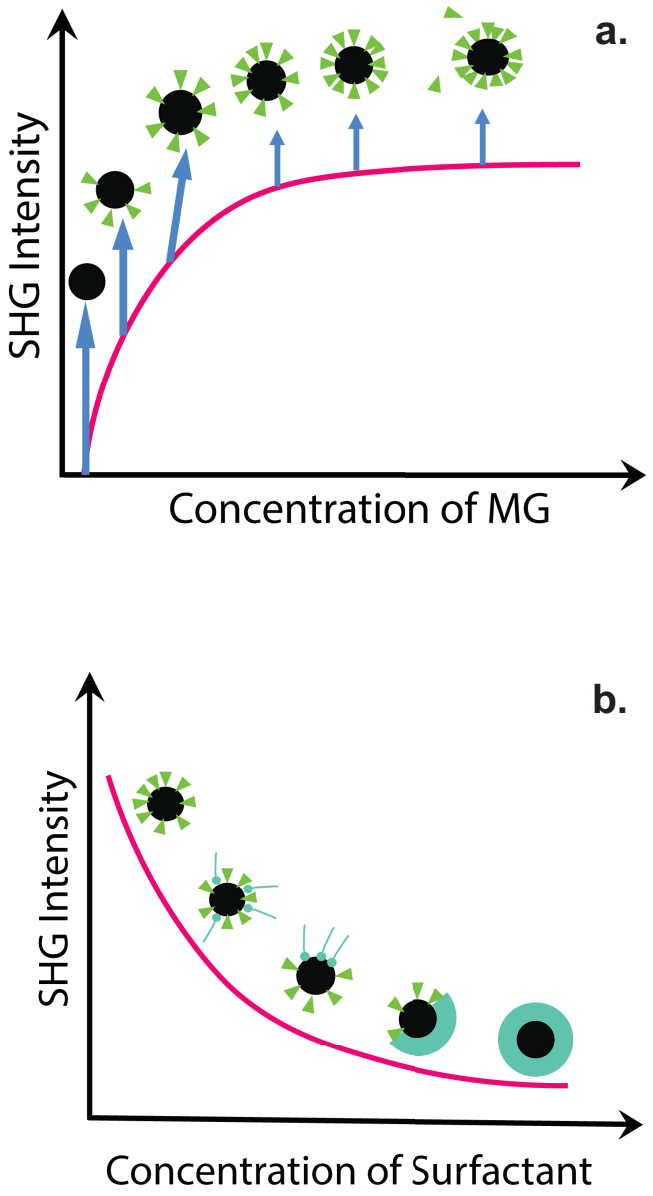


**Figure 5.1:** Schematic representation of (a) adsorption isotherm and (b) competitive adsorption isotherm data plots. (a) Shows how SHG intensity increases with increasing MG dye concentration. (b) Shows the decrease of the SHG signal with the increase of the surfactant concentration as the surfactant displaces the absorbed dye molecules

Figure 5.1 (b) represents the data plot of a competitive adsorption isotherm experiment where the SHG intensity is plotted as a function of surfactant concentration. At zero concentration of surfactant, the sample contains bead surfaces saturated with adsorbed MG dye molecule leading to a peak SHG signal. Gradual increase of surfactant concentration in the sample solution decreases the SHG signal as the surfactant molecules displace the adsorbed MG dye molecule from the surface. As the surfactant molecules are nonresonant with the SHG frequency, the adsorbed surfactant molecules will not produce a significant SHG signal compared with the signal from the adsorbed resonant MG dye molecules. Cole et al. (2019); Eckenrode et al. (2005) Fitting this decay of SHG signal with the competitive adsorption isotherm model, the adsorption energy of the surfactant and the number of active sites at which the surfactants are adsorbed can be extracted. Details of the calculation will be discussed in the following sections.

## 5.3 Results and Discussions

Before discussing the results obtained from this study, it is worth mentioning that the data analysis part is still ongoing. For this reason, the adsorption parameters of the molecules are not included here.

## 5.4 SHG from MG in a Microemulsion

We first attempted an adsorption isotherm of MG onto the polystyrene beads in a microemulsion environment. Our goal was to assess the ability of the small molecule to reach the charged surface in the microemulsion sample in which the most facile electron transfer was observed. Peng et al. (2020) In this experiment, $10^8$ PS beads per ml were dispersed a microemulsion made with toluene, Tween 20, butanol, and water as done in chapter 3. The overall weight percentage of water in this microemulsion was 60%. The pH of the water was 4.1.

Figure 5.2 shows that no change in SHG signal was detected as the MG stock solution was added to the sample. Our hypothesis is that the amount of surfactant presents in the 60% microemulsion is completely coating the PS bead surface preventing the MG from adsorpting in such a way that it can generate SHG. To further assess the surfactant-surface interaction, competitive isotherm experiments were conducted.

### 5.4.1 Adsorption Isotherm of MG in presence of Tween 20

As mentioned above, the parameters from adsorption isotherm experiments are needed for the fitting model of competitive adsorption isotherm. We collected the adsorption isotherms of MG with and without the presence of Tween 20 in the sample. Figure 5.3 shows the SHG intensity data plotted as a function of MG concentration for two sample scenarios. The black symbols represent the data points from the sample containing only PS beads and the red symbols represent the data points from the sample containing PS beads and 0.49 $\mu$M Tween 20. The figure shows that with the increase of MG concentration, the SHG intensity increases and reaches a plateau, but the intensity is not the same at which both the curves reach the plateau. The SHG intensity is dependent on the number of MG dyes adsorbed at the surface. The number of active sites at the bead surface is limited for MG dyes when Tween 20 is present in the sample because a partial portion of the surface is already covered with Tween 20.

### 5.4.2 Competitive Adsorption Isotherm of Nonionic Surfactants

Competitive adsorption isotherms collected via SHG have previously been reported in the literature to quantify the interaction between macromolecules and charged bead surfaces.

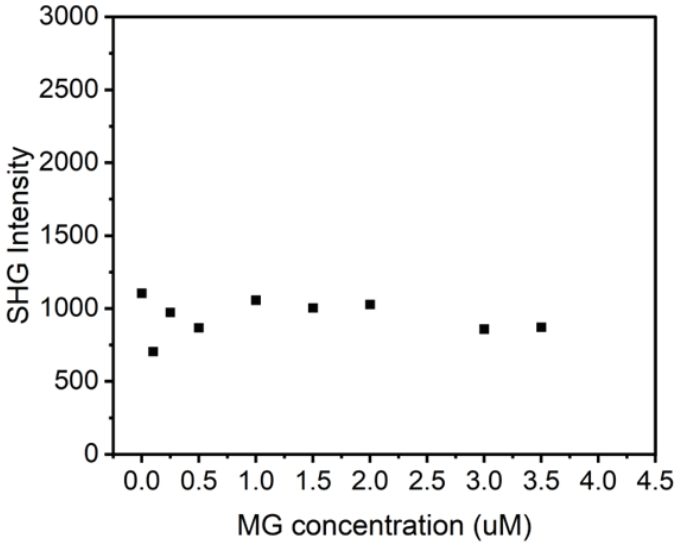


**Figure 5.2:** No SHG signal was observed from MG interacting with the polystyrene bead surface in the microemulsion

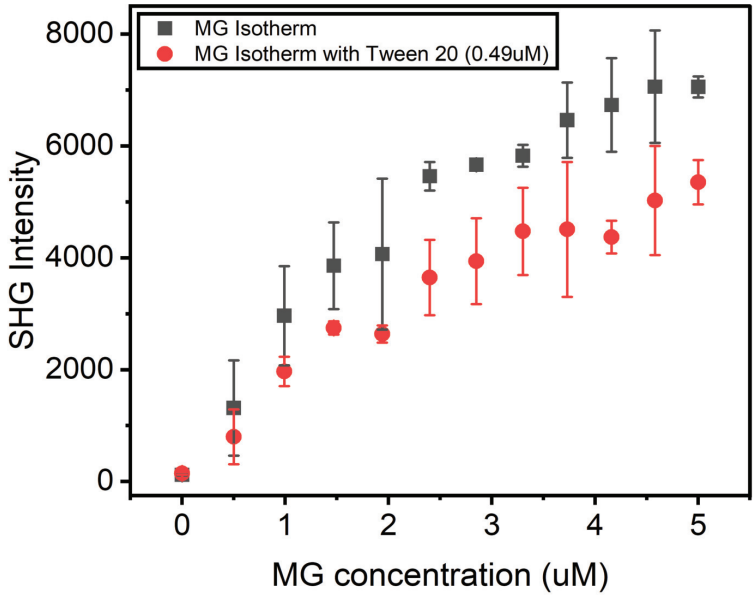


**Figure 5.3:** Adsorption isotherms of MG dye at PS bead surfaces with and without the presence of Tween 20 (0.49 $\mu$M) in the sample

In 2005, Eckenrode *et al.* employed employed SHG competitive adsorption isotherm to study the interaction biopolymers with negatively charged polystyrene beads. Eckenrode et al. (2005) In their experiment, they explored the adsorption mechanism of two poly-l-lysine polymers of different chain lengths , PL 14 (14 amino acid units) and PL 75 (75 amino acid units). Figure 5.4 shows the competitive adsorption isotherm of PL 14 and PL 75 from their study. The decay of the SHG signal from MG adsorbed at the bead surface shows that PL 75 requires less concentration to cover the PS bead surface and displace MG compared with PL 14. These results show how just a difference in the chain length of polymers can yield significantly different adsorption affinities to a charged surface.

Figure 5.5 shows competitive adsorption isotherms we collected of nonionic surfactants Tween 20 and BrijO20 at the negatively charged PS bead surface. In the figure, it is seen that the SHG signal is decreasing with the increase of the surfactant concentration. The surfactant molecules are displacing the adsorbed MG dye molecules from the bead surface. The decrease in intensity is different if we compare the SHG signal decays for both surfactants. Tween 20 causes a larger drop in SHG signal intensity with lower concentration than BrijO20. Although both of these surfactants are nonionic in nature, the structure of these surfactants differs, Figure 5.5 shows the structures of these surfactants. The most significant difference is in the polar region where Tween 20 has a larger, 3 chain headgroup while BrijO20's headgroup is a single chain. Regarding the nonpolar tails, BrijO20's is slightly longer. The faster decay of MG SHG signal observed for Tween 20 then likely arises from interactions between the surface and the headgroup. One likely mechanism could be hydrogen bonding with the increased number of OH groups in Tween. If we look closely at the figure, we can see that the SHG intensity is overall reduced by around 40% vs 50% by the Tween 20 and BrijO20. This indicates that these surfactants are adsorbed differently at the surface because after adsorption the number of sites available for MG is different for each case. Eckenrode et al. (2005)

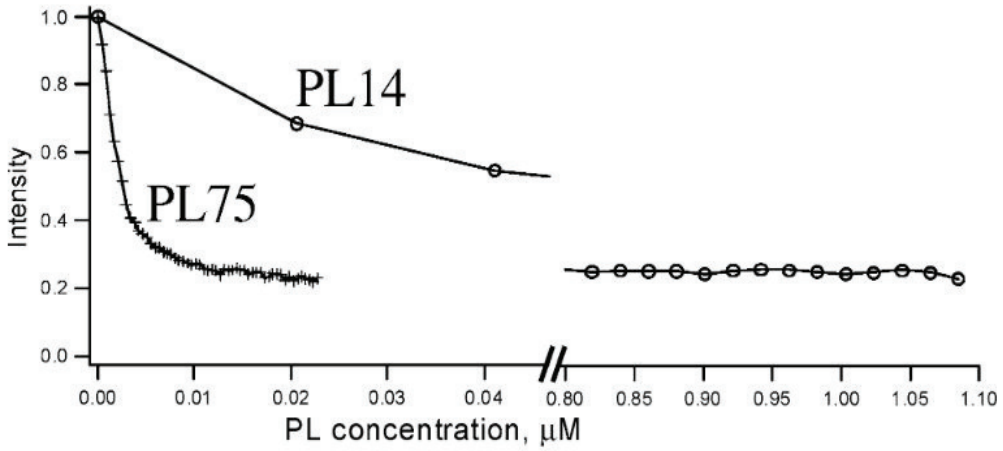


**Figure 5.4:** Comparison of the adsorption behavior of PL 75 and PL 14 on the negatively charged bead surface. The PL 75 requires less concentration to decrease the SHG signal comparing with PL 14. Eckenrode et al. (2005)

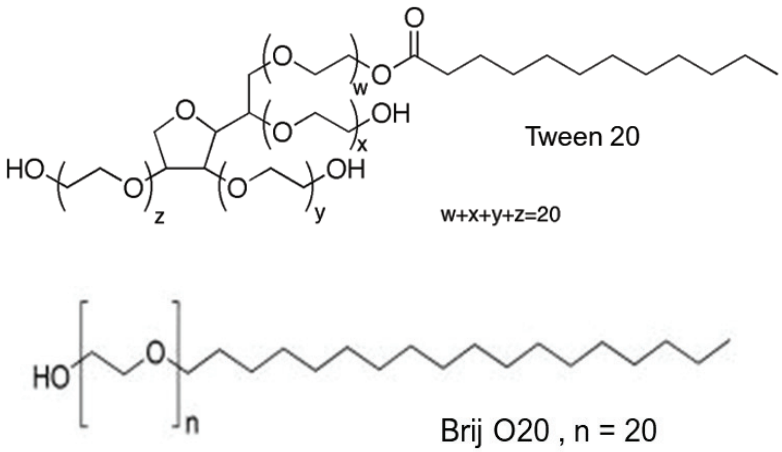


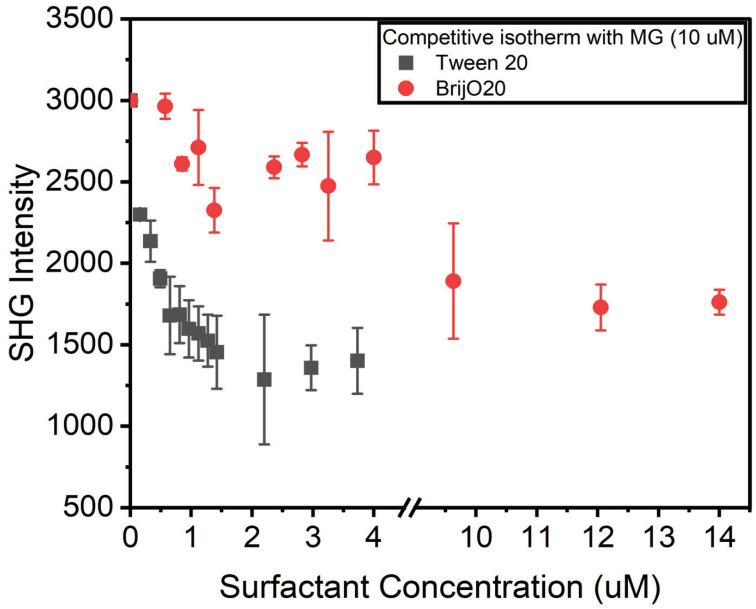


**Figure 5.5:** Competitive adsorption isotherms of Tween 20 and BrijO20, the SHG intensity decreases with the increase of the surfactant concentrations. Tween 20 decreases the SHG signal faster than BrijO20

If the intensity were reduced to the same percentage, the conclusion could have been drawn that both of the surfactants have adsorbed in a similar fashion, like what we have seen in the literature case study mentioned above. These results are important because the way a surfactant adsorbs at the active site may induce different mass transport rates.

### 5.4.3 Data Analysis For Future Studies

The SHG signal from the adsorbed resonant MG dye molecule can be defined by the coverage of the dye molecules at the surface,

$$I_{SHG} = B + [b + a\theta_D e^{i\phi}]^2 \tag{5.1}$$

where $I_{SHG}$ is the SHG signal intensity, $B$ is a constant representing the background contribution from nonresonant sources, $b$ is the bulk contribution of SHG from the particle, $a$ is a proportional constant contributing from the surface SHG, $\theta_D$ is the surface coverage by the dye molecules and $\phi$ is the phase factor of the signal interference from the surface and dye. The SHG signal is thus proportional to the square of surface coverage by the dye molecules. The surface coverage term of equation 5.1 depends on the total concentration of MG, $C_D$, and the maximum density of the adsorbed MG molecules $N^D_{max}$. The surface coverage can be further defined by the following equation,

$$\theta_D = [(C_D + N^D_{max} + 55.5/K_D) - [(C_D + N^D_{max} + 55.5/K_D)^2 - 4C_D N^D_{max}]^{0.5}]/2N^D_{max} \tag{5.2}$$

Here $K_D$ is the equilibrium constant for the adsorption of MG molecules at the surface and is defined as,

$$K_D = k_D^{-1}/k_D \tag{5.3}$$

$k_D^{-1}$ refers to the rate of MG desorption and $k_D$ refers to the rate of MG absorption at the bead surface. By fitting the SHG signal of MG isotherm without Tween 20 shown in Figure 5.3 with equations 5.1 and 5.2, the maximum absorbed density of MG, $N_{max}^D$, and the equilibrium constant, $K_D$, of MG dye can be extracted.

For competitive adsorption isotherm experiments, the sample contains adsorbed MG molecules and surfactant molecules fighting for the active sites of the bead surface. As such, two equilibria for the adsorption of MG and surfactant coexists. The surface coverage term, $\theta_D$, then becomes,

$$\theta_D = \frac{x}{1 + x + y} \tag{5.4}$$

where $x$ and $y$ are,

$$x = K_D(\frac{C_D - N_{max}^D}{55.5}) \tag{5.5}$$

$$y = K_S(\frac{C_S - N_{max}^S}{55.5}) \tag{5.6}$$

Here, $K_S$, $C_S$, and $N_{max}^S$ are the equilibrium constant, total concentration and maximum density of the absorbed surfactant molecules, respectively. Using the extracted values from the MG adsorption isotherm experiment, the counterpart surfactant term can be extracted. Wang et al. (2000)

## 5.5 Conclusions

The measurements in this chapter have been able to capture the impacts the adsorption of two nonionic surfactants, Tween 20 and BrijO20 at a negatively charged polystyrene particle surface with a home-built SHG spectroscopy instrument. Initial observations indicate that Tween 20 has a stronger adsorption affinity towards the charged surface compared with other nonionic surfactant, BrijO20. The adsorption

mechanism was likely influenced by hydrogen bonding of the hydrophilic part of these surfactant molecules. The results showed that such SHG measurements have the potential to be applied for the screening of surfactant molecules considered for electrolyte microemulsion formulation. After quantitative data analysis, the specific adsorption parameters of the molecules can be extracted.

# Chapter 6

# Conclusions and Future Outlook

## 6.1 Conclusions

In this dissertation, a fluorescence spectroscopy instrument capable of measuring time-resolved fluorescence events has been built. Employing this home-built instrument, time-resolved fluorescence anisotropy measurements of ionic(c153 and 4AP), polar(r6g), and non-polar(DPA) fluorophores dissolved in microemulsions and deep eutectic solvents have been collected. The anisotropy measurements of the above mentioned fluorophores in microemulsions captured the structural transition from bicontinuous to droplet phase. Measurements of the fluorophores dissolved in deep eutectic solvents suggested the hydrogen bonding network in this complex fluid is driven by the HBD molecules.

Various experiments employing steady-state fluorescence techniques have also being reported in this dissertation. Significant results from those experiment includes the showcase of the partitioning capability of Tween 20 in microemulsions, sensing the spatial heterogeneity in deep eutectic solvents, and the hydration of the surfactant layer in the microemulsions.

A second harmonic generation spectroscopy instrument was also built and used to study the adsorption of surfactants at a charged bead surface.

## 6.2 Future Outlook

The results of the rotational diffusion of the probe molecules in the microemulsion and deep eutectic solvents showcased the need for the measurement of translational diffusion of the probe molecules in those complex fluids. The translational diffusion of the probe molecules can be carried out with fluorescence correlation spectroscopy (FCS). Hossain and Samanta (2018); Das and Biswas (2015); Pal et al. (2011) Combining both rotational and translation diffusion of the fluorophore probes in these complex fluids will reveal the properties of the complex heterogeneous

microenvironments that exist. Complete characterization of these microenvironments will aid in designing new classes of electrolytes

The application of versatile fluorescence techniques can be employed to characterize other classes of complex fluids such as nanoparticle organic hybrid solvents.

An immediate research application for SHG spectroscopy would be to study the surfactant adsorption at various electrode surfaces. Bian et al. (2018); Bai et al.(2020)

# Bibliography

# Bibliography

(2006a). Fluorescence Anisotropy. In Lakowicz, J. R., editor, *Principles of Fluorescence Spectroscopy*. Springer US, Boston, MA. 13, 33, 54

(2006b). Introduction to Fluorescence. In Lakowicz, J. R., editor, *Principles of Fluorescence Spectroscopy*, pages 1–26. Springer US, Boston, MA. 16

Abbott, A. P., Capper, G., Davies, D. L., McKenzie, K. J., and Obi, S. U. (2006a). Solubility of Metal Oxides in Deep Eutectic Solvents Based on Choline Chloride. *J. Chem. Eng. Data*, 51(4):1280–1282. Publisher: American Chemical Society. 9

Abbott, A. P., Capper, G., Davies, D. L., Rasheed, R. K., and Tambyrajah, V. (2003). Novel solvent properties of choline chloride/urea mixtures. *Chem. Commun.*, (1):70–71. Publisher: The Royal Society of Chemistry. 8, 9, 49

Abbott, A. P., Capper, G., and Gray, S. (2006b). Design of Improved Deep Eutectic Solvents Using Hole Theory. *ChemPhysChem*, 7(4):803–806. _eprint: https://onlinelibrary.wiley.com/doi/pdf/10.1002/cphc.200500489. 9

Abbott, A. P., Capper, G., McKenzie, K. J., and Ryder, K. S. (2007). Electrodeposition of zinc–tin alloys from deep eutectic solvents based on choline chloride. *Journal of Electroanalytical Chemistry*, 599(2):288–294. 49

Adhikari, A., Sahu, K., Dey, S., Ghosh, S., Mandal, U., and Bhattacharyya, K. (2007). Femtosecond solvation dynamics in a neat ionic liquid and ionic liquid

microemulsion: excitation wavelength dependence. *J Phys Chem B*, 111(44):12809–16. 35, 40

Bai, R., Xue, M., Lin, Y., Wen, R., Guo, Y., and Zhang, Z. (2020). Adsorption and Oxidation Dynamics of Disperse Orange 3 on a Polycrystalline Pt Electrode Studied by In Situ Second Harmonic Generation. *J. Phys. Chem. C*, 124(39):21625–21634. Publisher: American Chemical Society. 83

Bain, A. J., Chandna, P., Butcher, G., and Bryant, J. (2000). Picosecond polarized fluorescence studies of anisotropic fluid media. II. Experimental studies of molecular order and motion in jet aligned rhodamine 6G and resorufin solutions. *The Journal of Chemical Physics*, 112(23):10435–10449. 40

Barth, B. A., Imel, A., Nelms, K. M., Goenaga, G. A., and Zawodzinski, T. (2022). Microemulsions: Breakthrough Electrolytes for Redox Flow Batteries. *Frontiers in Chemistry*, 10. 2, 4

Bartolozzi, M. (1989). Development of redox flow batteries. A historical bibliography. *Journal of Power Sources*, 27(3):219–234. 2

Ben-Amotz, D. and Scott, T. W. (1987). Microscopic frictional forces on molecular motion in liquids. Picosecond rotational diffusion in alkanes and alcohols. *The Journal of Chemical Physics*, 87(7):3739–3748. 44

Bera, N., Ghosh, M., Nandi, S., and Sarkar, N. (2021). Femtosecond solvation dynamics study of hydrophobic and hydrophilic probes in various room temperature ionic liquids (RTILs) containing microemulsions. *Chemical Physics Letters*, 767:138356. 35

Bian, H.-t., Guo, Y., and Wang, H.-f. (2018). Non-parabolic potential dependence of optical second harmonic generation from the Si(111) electrode/electrolyte interface. *Phys. Chem. Chem. Phys.*, 20(46):29539–29548. Publisher: The Royal Society of Chemistry. 83

Blackburn, F. R., Wang, C.-Y., and Ediger, M. D. (1996). Translational and Rotational Motion of Probes in Supercooled 1,3,5-Tris(naphthyl)benzene. *The Journal of Physical Chemistry*, 100(46):18249–18257. 40

Boyd, R. W. (2020). *Nonlinear Optics*. Academic Press. Google-Books-ID: 54vZDwAAQBAJ. 12, 13, 19

Carnero Ruiz, C., Hierrezuelo, J. M., and Molina-Bolívar, J. A. (2017). Effect of the micellar composition on the rotational relaxation dynamics of Coumarin 153 in mixed micelles of n-dodecyl--d-maltoside and sodium dodecyl sulfate. *Journal of Luminescence*, 192:188–195. 40

Chakrabarty, D., Seth, D., Chakraborty, A., and Sarkar, N. (2005). Dynamics of Solvation and Rotational Relaxation of Coumarin 153 in Ionic Liquid Confined Nanometer-Sized Microemulsions. *The Journal of Physical Chemistry B*, 109(12):5753–5758. 27, 35

Chen, V., Warr, G. G., Evans, D. F., and Prendergast, F. G. (1988). Curvature and geometric constraints as determinants of microemulsion structure: evidence from fluorescence anisotropy measurements. *The Journal of Physical Chemistry*, 92(3):768–773. 26, 27

Chern, C. S. (2006). Emulsion polymerization mechanisms and kinetics. *Progress in Polymer Science*, 31(5):443–486. 25

Cole, W. T. S., Wei, H., Nguyen, S. C., Harris, C. B., Miller, D. J., and Saykally, R. J. (2019). Dynamics of Micropollutant Adsorption to Polystyrene Surfaces Probed by Angle-Resolved Second Harmonic Scattering. *J. Phys. Chem. C*, 123(23):14362–14369. Publisher: American Chemical Society. 69, 71

Das, A. and Biswas, R. (2015). Dynamic Solvent Control of a Reaction in Ionic Deep Eutectic Solvents: Time-Resolved Fluorescence Measurements of Reactive

and Nonreactive Dynamics in (Choline Chloride + Urea) Melts. *J. Phys. Chem. B*, 119(31):10102–10113. Publisher: American Chemical Society. 50, 54, 56, 82

Das, A., Das, S., and Biswas, R. (2015). Density relaxation and particle motion characteristics in a non-ionic deep eutectic solvent (acetamide + urea): Time-resolved fluorescence measurements and all-atom molecular dynamics simulations. *J. Chem. Phys.*, 142(3):034505. Publisher: American Institute of Physics. 50, 56

Dayalan, E., Qutubuddin, S., and Hussam, A. (2002). Electrochemical investigations in microemulsion media. 1. Methylviologen reduction. *Langmuir*, 6(4):715–721. 26

Denholm, P., Fernandez, S., Hall, D., Mai, T., and Tegen, S. (2012). Energy storage technologies. *Orgs.). Grid Energy Storage: Benefits*. 2

Dhingra, D., Bhawna, Pandey, A., and Pandey, S. (2019). Pyrene Fluorescence To Probe a Lithium Chloride-Added (Choline Chloride + Urea) Deep Eutectic Solvent. *J. Phys. Chem. B*, 123(14):3103–3111. Publisher: American Chemical Society. 49

Domínguez de María, P. and Maugeri, Z. (2011). Ionic liquids in biotransformations: from proof-of-concept to emerging deep-eutectic-solvents. *Current Opinion in Chemical Biology*, 15(2):220–225. 49

Doughty, D. H., Butler, P. C., Akhil, A. A., Clark, N. H., and Boyes, J. D. (2010). Batteries for Large-Scale Stationary Electrical Energy Storage. *Electrochem. Soc. Interface*, 19(3):49. Publisher: IOP Publishing. 2

Duncan, K. M., Casey, A., Gobrogge, C. A., Trousdale, R. C., Piontek, S. M., Cook, M. J., Steel, W. H., and Walker, R. A. (2020). Coumarin Partitioning in Model Biological Membranes: Limitations of log P as a Predictor. *The Journal of Physical Chemistry B*, 124(38):8299–8308. 37

Durand, E., Lecomte, J., and Villeneuve, P. (2013). Deep eutectic solvents: Synthesis, application, and focus on lipase-catalyzed reactions.

*European Journal of Lipid Science and Technology*, 115(4):379–385. _eprint: https://onlinelibrary.wiley.com/doi/pdf/10.1002/ejlt.201200416. 49

Eckenrode, H. M. and Dai, H.-L. (2004). Nonlinear Optical Probe of Biopolymer Adsorption on Colloidal Particle Surface: Poly-l-lysine on Polystyrene Sulfate Microspheres. *Langmuir*, 20(21):9202–9209. Publisher: American Chemical Society. 69

Eckenrode, H. M., Jen, S.-H., Han, J., Yeh, A.-G., and Dai, H.-L. (2005). Adsorption of a Cationic Dye Molecule on Polystyrene Microspheres in Colloids: Effect of Surface Charge and Composition Probed by Second Harmonic Generation. *J. Phys. Chem. B*, 109(10):4646–4653. Publisher: American Chemical Society. xiii, 68, 69, 71, 75, 76

Eisenthal, K. B. (2006). Second Harmonic Spectroscopy of Aqueous Nano- and Microparticle Interfaces. *Chem. Rev.*, 106(4):1462–1477. Publisher: American Chemical Society. 67, 69

Evans, D. F., Mitchell, D. J., and Ninham, B. W. (1984). Ion binding and dressed micelles. *J. Phys. Chem.*, 88(25):6344–6348. 8

Fleming, G. R. and Fleming, P. o. C. G. R. (1986). *Chemical Applications of Ultrafast Spectroscopy*. Oxford University Press. Google-Books-ID: JDZRAAAAMAAJ. 61

Funston, A. M., Fadeeva, T. A., Wishart, J. F., and Castner, E. W. (2007). Fluorescence Probing of Temperature-Dependent Dynamics and Friction in Ionic Liquid Local Environments. *The Journal of Physical Chemistry B*, 111(18):4963–4977. 40

Ganguli, A. K., Ganguly, A., and Vaidya, S. (2010). Microemulsion-based synthesis of nanocrystalline materials. *Chemical Society Reviews*, 39(2):474–485. 25

García, G., Aparicio, S., Ullah, R., and Atilhan, M. (2015). Deep Eutectic Solvents: Physicochemical Properties and Gas Separation Applications. *Energy Fuels*, 29(4):2616–2644. Publisher: American Chemical Society. 49

Ghatak, C., Rao, V. G., Pramanik, R., Sarkar, S., and Sarkar, N. (2011). The effect of membrane fluidity on FRET parameters: an energy transfer study inside small unilamellar vesicle. *Phys Chem Chem Phys*, 13(9):3711–20. 37

Guchhait, B., Al Rasid Gazi, H., Kashyap, H. K., and Biswas, R. (2010). Fluorescence Spectroscopic Studies of (Acetamide + Sodium/Potassium Thiocyanates) Molten Mixtures: Composition and Temperature Dependence. *J. Phys. Chem. B*, 114(15):5066–5081. Publisher: American Chemical Society. 50

Gumy, J.-C. and Vauthey, E. (1996). Picosecond Polarization Grating Study of the Effect of Excess Excitation Energy on the Rotational Dynamics of Rhodamine 6G in Different Electronic States. *The Journal of Physical Chemistry*, 100(21):8628–8632. 19, 40

Guo, W., Hou, Y., Ren, S., Tian, S., and Wu, W. (2013). Formation of Deep Eutectic Solvents by Phenols and Choline Chloride and Their Physical Properties. *J. Chem. Eng. Data*, 58(4):866–872. Publisher: American Chemical Society. 61, 62

G. Overbeek, J. T. (1978). The First Rideal Lecture. Microemulsions, a field at the border between lyophobic and lyophilic colloids. *Faraday Discussions of the Chemical Society*, 65(0):7–19. Publisher: Royal Society of Chemistry. 6

Hansen, B. B., Spittle, S., Chen, B., Poe, D., Zhang, Y., Klein, J. M., Horton, A., Adhikari, L., Zelovich, T., Doherty, B. W., Gurkan, B., Maginn, E. J., Ragauskas, A., Dadmun, M., Zawodzinski, T. A., Baker, G. A., Tuckerman, M. E., Savinell, R. F., and Sangoro, J. R. (2021). Deep Eutectic Solvents: A Review of Fundamentals and Applications. *Chem. Rev.*, 121(3):1232–1285. Publisher: American Chemical Society. 8, 9, 49, 50

Hoar, T. P. and Schulman, J. H. (1943). Transparent Water-in-Oil Dispersions: the Oleopathic Hydro-Micelle. *Nature*, 152(3847):102–103. Number: 3847 Publisher: Nature Publishing Group. 5

Horng, M. L., Gardecki, J. A., and Maroncelli, M. (1997). Rotational Dynamics of Coumarin 153: Time-Dependent Friction, Dielectric Friction, and Other Nonhydrodynamic Effects. *The Journal of Physical Chemistry A*, 101(6):1030–1047. 32, 33, 37, 40, 53

Horng, M. L., Gardecki, J. A., Papazyan, A., and Maroncelli, M. (1995). Subpicosecond Measurements of Polar Solvation Dynamics: Coumarin 153 Revisited. *The Journal of Physical Chemistry*, 99(48):17311–17337. 19, 35

Hossain, S. S., Paul, S., and Samanta, A. (2019). Liquid Structure and Dynamics of Tetraalkylammonium Bromide-Based Deep Eutectic Solvents: Effect of Cation Chain Length. *J. Phys. Chem. B*, 123(31):6842–6850. Publisher: American Chemical Society. 50, 54, 56, 57

Hossain, S. S., Paul, S., and Samanta, A. (2020). Complete Solvation Dynamics of Coumarin 153 in Tetraalkylammonium Bromide-Based Deep Eutectic Solvents. *J. Phys. Chem. B*, 124(12):2473–2481. Publisher: American Chemical Society. 50

Hossain, S. S. and Samanta, A. (2017). Solute Rotation and Translation Dynamics in an Ionic Deep Eutectic Solvent Based on Choline Chloride. *J. Phys. Chem. B*, 121(46):10556–10565. Publisher: American Chemical Society. 56, 57, 62

Hossain, S. S. and Samanta, A. (2018). How do the hydrocarbon chain length and hydroxyl group position influence the solute dynamics in alcohol-based deep eutectic solvents? *Phys. Chem. Chem. Phys.*, 20(38):24613–24622. Publisher: The Royal Society of Chemistry. 54, 56, 57, 62, 82

Huang, Q., Yu, H., and Ru, Q. (2010). Bioavailability and Delivery of Nutraceuticals Using Nanotechnology. *Journal of Food Science*, 75(1):R50–R57. 25

Imel, A. E., Barth, B., Hayes, D. G., Dadmun, M., and Zawodzinski, T. (2022). Microemulsions as Emerging Electrolytes: The Correlation of Structure to Electrochemical Response. *ACS Applied Materials & Interfaces*, 14(17):20179–20189. 4, 42

Israelachvili, J. (1994). The science and applications of emulsions — an overview. *Colloids and Surfaces A: Physicochemical and Engineering Aspects*, 91:1–8. 5, 6, 8, 66

Iwunze, M. O., Sucheta, A., and Rusling, J. F. (1990). Bicontinuous microemulsions as media for electrochemical studies. *Analytical Chemistry*, 62(6):644–649. 26

Jen, S.-H. and Dai, H.-L. (2006). Probing Molecules Adsorbed at the Surface of Nanometer Colloidal Particles by Optical Second-Harmonic Generation. *J. Phys. Chem. B*, 110(46):23000–23003. Publisher: American Chemical Society. 67

Jen, S.-H., Gonella, G., and Dai, H.-L. (2009). The Effect of Particle Size in Second Harmonic Generation from the Surface of Spherical Colloidal Particles. I: Experimental Observations. *J. Phys. Chem. A*, 113(16):4758–4762. Publisher: American Chemical Society. 67, 69

Jha, B. K., Kulkarni, B. D., Vinod, M. P., and Vijayamohanan, K. (1995). An unusual electron-transfer behavior of ferrocene in aqueous microemulsion systems. *Chemical Physics Letters*, 240(5):442–448. 26

Jin, H., Baker, G. A., Arzhantsev, S., Dong, J., and Maroncelli, M. (2007). Solvation and Rotational Dynamics of Coumarin 153 in Ionic Liquids: Comparisons to Conventional Solvents. *The Journal of Physical Chemistry B*, 111(25):7291–7302. 37

Kadyan, A., Behera, K., and Pandey, S. (2016). Hybrid green nonaqueous media: tetraethylene glycol modifies the properties of a (choline chloride + urea) deep

eutectic solvent. *RSC Adv.*, 6(36):29920–29930. Publisher: The Royal Society of Chemistry. 49

Kadyan, A., Juneja, S., and Pandey, S. (2019). Photophysical Behavior and Fluorescence Quenching of l-Tryptophan in Choline Chloride-Based Deep Eutectic Solvents. *J. Phys. Chem. B*, 123(35):7578–7587. Publisher: American Chemical Society. 50

Khan, M. F., Singh, M. K., and Sen, S. (2016). Measuring Size, Size Distribution, and Polydispersity of Water-in-Oil Microemulsion Droplets using Fluorescence Correlation Spectroscopy: Comparison to Dynamic Light Scattering. *The Journal of Physical Chemistry B*, 120(5):1008–1020. 27

Kunieda, H. and Shinoda, K. (1980). Solution behavior and hydrophile-lipophile balance temperature in the aerosol OT-isooctane-brine system: Correlation between microemulsions and ultralow interfacial tensions. *Journal of Colloid and Interface Science*, 75(2):601–606. 6

Kunitake, M., Kuraya, E., Kato, D., Niwa, O., and Nishimi, T. (2016). Electrochemistry in bicontinuous microemulsions based on control of dynamic solution structures on electrode surfaces. *Current Opinion in Colloid & Interface Science*, 25:13–26. 26

Laia, C. A. T. and Costa, S. M. B. (2002). Rotational Friction in AOT Microemulsions: Relevance of Hydrodynamic and Dielectric Contributions to Microviscosities Probed by Fluorescent Bis[4-(dimethylamino)phenyl] Squaraine. *Langmuir*, 18(5):1494–1504. 27

Leng, L., Li, H., Yuan, X., Zhou, W., and Huang, H. (2018). Bio-oil upgrading by emulsification/microemulsification: A review. *Energy*, 161:214–232. 25

Li, L., Chang, M., Yi, H., Jia, M., Cao, X., Zhou, Z., Zhang, S., Pan, H., Shih, C.-W., Jimenez, R., and Xu, J. (2016). Using Pyridinium Styryl Dyes as the Standards

of Time-Resolved Instrument Response. *Applied Spectroscopy*, 70(7):1195–1201. 2, 17, 32, 53

Lissi, E. A., Abuin, E. B., Rubio, M. A., and Cerón, A. (2000). Fluorescence of Prodan and Laurdan in AOT/Heptane/Water Microemulsions: Partitioning of the Probes and Characterization of Microenvironments†. *Langmuir*, 16(1):178–181. 26, 27, 35

Loow, Y.-L., Wu, T. Y., Yang, G. H., Ang, L. Y., New, E. K., Siow, L. F., Md. Jahim, J., Mohammad, A. W., and Teoh, W. H. (2018). Deep eutectic solvent and inorganic salt pretreatment of lignocellulosic biomass for improving xylose recovery. *Bioresource Technology*, 249:818–825. 49

Luo, J., Hu, B., Debruler, C., Bi, Y., Zhao, Y., Yuan, B., Hu, M., Wu, W., and Liu, T. L. (2019a). Unprecedented Capacity and Stability of Ammonium Ferrocyanide Catholyte in pH Neutral Aqueous Redox Flow Batteries. *Joule*, 3(1):149–163. 4

Luo, J., Hu, B., Hu, M., Zhao, Y., and Liu, T. L. (2019b). Status and Prospects of Organic Redox Flow Batteries toward Sustainable Energy Storage. *ACS Energy Lett.*, 4(9):2220–2240. Publisher: American Chemical Society. 4

López-Quintela, M. A. (2003). Synthesis of nanomaterials in microemulsions: formation mechanisms and growth control. *Current Opinion in Colloid & Interface Science*, 8(2):137–144. 25

Mackay, R. A. (1991). Electrochemistry of solutes in microemulsions: Electrostatically bound aqueous ions, surfactant-like ions and oil soluble molecules. *Colloids and Surfaces*, 56:1–12. 4, 26

MacKay, R. A. and Agarwal, R. (1978). Conductivity measurements in nonionic microemulsions. *Journal of Colloid and Interface Science*, 65(2):225–231. 5, 26

Mackay, R. A., Myers, S. A., and Brajter-Toth, A. (1996). Interpreting diffusion coefficients of electrochemical probes in oil-in-water microemulsions. *Electroanalysis*, 8(8-9):759–764. 26

Mano, F., Martins, M., Sá-Nogueira, I., Barreiros, S., Borges, J. P., Reis, R. L., Duarte, A. R. C., and Paiva, A. (2017). Production of Electrospun Fast-Dissolving Drug Delivery Systems with Therapeutic Eutectic Systems Encapsulated in Gelatin. *AAPS PharmSciTech*, 18(7):2579–2585. 49

Maroncelli, M. and Fleming, G. R. (1987). Picosecond solvation dynamics of coumarin 153: The importance of molecular aspects of solvation. *The Journal of Chemical Physics*, 86(11):6221–6239. 40

McClements, D. J. (2012). Nanoemulsions versus microemulsions: terminology, differences, and similarities. *Soft Matter*, 8(6):1719–1729. 5, 6, 26

McClements, D. J. and Rao, J. (2011). Food-grade nanoemulsions: formulation, fabrication, properties, performance, biological fate, and potential toxicity. *Crit Rev Food Sci Nutr*, 51(4):285–330. Number: 4. 5, 8, 66

Oliveira, M. E. C. D. R., Hungerford, G., Miguel, M. d. G., and Burrows, H. D. (2001). Solvatochromic fluorescent probes in bicontinuous microemulsions. *Journal of Molecular Structure*, 563-564:443–447. 27, 40

Pal, M., Rai, R., Yadav, A., Khanna, R., Baker, G. A., and Pandey, S. (2014). Self-Aggregation of Sodium Dodecyl Sulfate within (Choline Chloride + Urea) Deep Eutectic Solvent. *Langmuir*, 30(44):13191–13198. Publisher: American Chemical Society. 49

Pal, N., Dev Verma, S., Singh, M. K., and Sen, S. (2011). Fluorescence correlation spectroscopy: an efficient tool for measuring size, size-distribution and polydispersity of microemulsion droplets in solution. *Anal Chem*, 83(20):7736–44. 27, 82

Pandey, A., Bhawna, Dhingra, D., and Pandey, S. (2017). Hydrogen Bond Donor/Acceptor Cosolvent-Modified Choline Chloride-Based Deep Eutectic Solvents. *J. Phys. Chem. B*, 121(16):4202–4212. Publisher: American Chemical Society. 50

Pandey, A., Rai, R., Pal, M., and Pandey, S. (2013). How polar are choline chloride-based deep eutectic solvents? *Phys. Chem. Chem. Phys.*, 16(4):1559–1568. Publisher: The Royal Society of Chemistry. 50

Parasassi, T., De Stasio, G., Ravagnan, G., Rusch, R. M., and Gratton, E. (1991). Quantitation of lipid phases in phospholipid vesicles by the generalized polarization of Laurdan fluorescence. *Biophysical Journal*, 60(1):179–189. 35

Parasassi, T., Di Stefano, M., Loiero, M., Ravagnan, G., and Gratton, E. (1994). Influence of cholesterol on phospholipid bilayers phase domains as detected by Laurdan fluorescence. *Biophysical Journal*, 66(1):120–132. 27, 31, 33

Peng, J., Cantillo, N. M., Nelms, K. M., Roberts, L. S., Goenaga, G., Imel, A., Barth, B. A., Dadmun, M., Heroux, L., Hayes, D. G., and Zawodzinski, T. (2020). Electron Transfer in Microemulsion-Based Electrolytes. *ACS Appl Mater Interfaces*, 12(36):40213–40219. 5, 26, 27, 28, 42, 66, 71

Philips, L. A., Webb, S. P., and Clark, J. H. (1985). High-pressure studies of rotational reorientation dynamics: The role of dielectric friction. *The Journal of Chemical Physics*, 83(11):5810–5821. 40

Porel, M., Chuang, C.-H., Burda, C., and Ramamurthy, V. (2012). Ultrafast Photoinduced Electron Transfer between an Incarcerated Donor and a Free Acceptor in Aqueous Solution. *Journal of the American Chemical Society*, 134(36):14718–14721. 39

Pramanik, R., Sarkar, S., Ghatak, C., Setua, P., and Sarkar, N. (2010). Effect of polymer , poly(ethylene glycol)(PEG-400), on solvent and rotational relaxation of

coumarin-480 in an ionic liquid containing microemulsions. *Physical Chemistry Chemical Physics*, 12(15):3878–3886. 27

Prince, L. M. (1967). A theory of aqueous emulsions I. Negative interfacial tension at the oil/water interface. *Journal of Colloid and Interface Science*, 23(2):165–173. 66

P. Abbott, A., M. Cullis, P., J. Gibson, M., C. Harris, R., and Raven, E. (2007). Extraction of glycerol from biodiesel into a eutectic based ionic liquid. *Green Chemistry*, 9(8):868–872. Publisher: Royal Society of Chemistry. 9

Rao, J. and McClements, D. J. (2011). Food-grade microemulsions, nanoemulsions and emulsions: Fabrication from sucrose monopalmitate & lemon oil. *Food Hydrocolloids*, 25(6):1413–1423. 5

Rao, V. G., Mandal, S., Ghosh, S., Banerjee, C., and Sarkar, N. (2012). Ionic Liquid-in-Oil Microemulsions Composed of Double Chain Surface Active Ionic Liquid as a Surfactant: Temperature Dependent Solvent and Rotational Relaxation Dynamics of Coumarin-153 in [Py][TF2N]/[C4mim][AOT]/Benzene Microemulsions. *The Journal of Physical Chemistry B*, 116(28):8210–8221. 27

Reed, M., Johansen, O., Brandvik, P. J., Daling, P., Lewis, A., Fiocco, R., Mackay, D., and Prentki, R. (1999). Oil Spill Modeling towards the Close of the 20th Century: Overview of the State of the Art. *Spill Science & Technology Bulletin*, 5(1):3–16. 25

Reuter, D., Münzner, P., Gainaru, C., Lunkenheimer, P., Loidl, A., and Böhmer, R. (2021). Translational and reorientational dynamics in deep eutectic solvents. *J. Chem. Phys.*, 154(15):154501. Publisher: American Institute of Physics. 56

Reynolds, L., Gardecki, J. A., Frankland, S. J. V., Horng, M. L., and Maroncelli, M. (1996). Dipole Solvation in Nondipolar Solvents: Experimental Studies

of Reorganization Energies and Solvation Dynamics. *The Journal of Physical Chemistry*, 100(24):10337–10354. 37

Rusling, J. F. (2007). Electrochemistry in Micelles and Microemulsions. In *Encyclopedia of Electrochemistry*. American Cancer Society. 26

Sahu, K., Ghosh, S., Mondal, S. K., Ghosh, B. C., Sen, P., Roy, D., and Bhattacharyya, K. (2006). Ultrafast fluorescence resonance energy transfer in a micelle. *J Chem Phys*, 125(4):44714. 37

Sakuragi, M., Tsutsumi, S., and Kusakabe, K. (2018). Deep Eutectic Solvent-Induced Structural Transition of Microemulsions Explored with Small-Angle X-ray Scattering. *Langmuir*, 34(42):12635–12641. Publisher: American Chemical Society. 50

Schramm, L. L. (1992). Petroleum Emulsions. In *Emulsions*, volume 231 of *Advances in Chemistry*. American Chemical Society. 5, 25

Schulman, J. H., Stoeckenius, W., and Prince, L. M. (1959). Mechanism of Formation and Structure of Micro Emulsions by Electron Microscopy. *J. Phys. Chem.*, 63(10):1677–1680. Publisher: American Chemical Society. 5, 26

Seth, D., Chakraborty, A., Setua, P., and Sarkar, N. (2006). Interaction of Ionic Liquid with Water in Ternary Microemulsions (Triton X-100/Water/1-Butyl-3-methylimidazolium Hexafluorophosphate) Probed by Solvent and Rotational Relaxation of Coumarin 153 and Coumarin 151. *Langmuir*, 22(18):7768–7775. 27

Shah, D. M., Davies, K. M., and Hussam, A. (1997). Electrochemical Investigation of Amphiphilic Cobalt(III) Complexes and Ferrocene Derivatives in Sodium Dodecyl Sulfate Microemulsions. *Langmuir*, 13(17):4729–4736. 26

Shakeel, F., Ramadan, W., Faisal, M. S., Rizwan, M., Faiyazuddin, M., Mustafa, G., and Shafiq, S. (2010). Transdermal and Topical Delivery of Anti-inflammatory

Agents Using Nanoemulsion/Microemulsion: An Updated Review. *Current Nanoscience*, 6(2):184–198. 25

Shen, X., Sinclair, N., Wainright, J., Imel, A., Barth, B., Zawodzinski, T., and Savinell, R. F. (2021). A Study of Ferrocene Diffusion in Toluene/Tween 20/1-Butanol/Water Microemulsions for Redox Flow Battery Applications. *Journal of The Electrochemical Society*, 168(6):060539. 27

Singha, D., Sahu, D. K., and Sahu, K. (2018). Anomalous Spectral Modulation of 4-Aminophthalimide inside Acetonitrile/AOT/ n-Heptane Microemulsion: New Insights on Reverse Micelle to Bicontinuous Microemulsion Transition. *J Phys Chem B*, 122(27):6966–6974. 26, 27

Sjöblom, J., Lindberg, R., and Friberg, S. E. (1996). Microemulsions — phase equilibria characterization, structures, applications and chemical reactions. *Advances in Colloid and Interface Science*, 65:125–287. 8, 25, 66

Smith, E. L., Abbott, A. P., and Ryder, K. S. (2014). Deep Eutectic Solvents (DESs) and Their Applications. *Chem. Rev.*, 114(21):11060–11082. Publisher: American Chemical Society. 8, 9, 49

Soloveichik, G. L. (2015a). Flow Batteries: Current Status and Trends. *Chem. Rev.*, 115(20):11533–11558. Publisher: American Chemical Society. 2

Soloveichik, G. L. (2015b). Flow Batteries: Current Status and Trends. *Chemical Reviews*, 115(20):11533–11558. _eprint: https://doi.org/10.1021/cr500720t. 66

Srinivas, G. and Bagchi, B. (2001). Effect of Orientational Motion of Mobile Chromophores on the Dynamics of Förster Energy Transfer in Polymers. *The Journal of Physical Chemistry B*, 105(38):9370–9374. 39

Stefanovic, R., Ludwig, M., Webber, G. B., Atkin, R., and Page, A. J. (2017). Nanostructure, hydrogen bonding and rheology in choline chloride deep eutectic

solvents as a function of the hydrogen bond donor. *Phys. Chem. Chem. Phys.*, 19(4):3297–3306. Publisher: The Royal Society of Chemistry. 62

Stevens, C. E. (1957). Nonionic surfactants. *Journal of the American Oil Chemists' Society*, 34(4):181–185. 26

Strey, R. (1994). Microemulsion microstructure and interfacial curvature. *Colloid and Polymer Science*, 272(8):1005–1019. 26

Stumm, W. and Morgan, J. J. (1996). *Aquatic Chemistry: Chemical Equilibria and Rates in Natural Waters*. John Wiley & Sons, New York, 3 edition. 25

Subba, N., Tarif, E., Sen, P., and Biswas, R. (2020). Subpicosecond Solvation Response and Partial Viscosity Decoupling of Solute Diffusion in Ionic Acetamide Deep Eutectic Solvents: Fluorescence Up-Conversion and Fluorescence Correlation Spectroscopic Measurements. *J. Phys. Chem. B*, 124(10):1995–2005. Publisher: American Chemical Society. 49, 50, 54, 56, 57

Söldner, A., Zach, J., and König, B. (2019). Deep eutectic solvents as extraction media for metal salts and oxides exemplarily shown for phosphates from incinerated sewage sludge ash. *Green Chem.*, 21(2):321–328. Publisher: The Royal Society of Chemistry. 49, 50

Tarif, E., Mondal, J., and Biswas, R. (2019). Interaction and Dynamics in a Fully Biodegradable Glucose-Containing Naturally Abundant Deep Eutectic Solvent: Temperature-Dependent Time-Resolved Fluorescence Measurements. *J. Phys. Chem. B*, 123(44):9378–9387. Publisher: American Chemical Society. 56

Turner, A. H. and Kim, D. (2018). Rotation and translation dynamics of coumarin 153 in choline chloride-based deep eutectic solvents. *J. Chem. Phys.*, 149(17):174503. Publisher: American Institute of Physics. 50

Velikov, K. P. and Pelan, E. (2008). Colloidal delivery systems for micronutrients and nutraceuticals. *Soft Matter*, 4(10):1964–1980. 25

Vittal, R., Gomathi, H., and Kim, K.-J. (2006). Beneficial role of surfactants in electrochemistry and in the modification of electrodes. *Advances in Colloid and Interface Science*, 119(1):55–68. 66

Wagle, D. V., Zhao, H., and Baker, G. A. (2014). Deep Eutectic Solvents: Sustainable Media for Nanoscale and Functional Materials. *Acc. Chem. Res.*, 47(8):2299–2308. Publisher: American Chemical Society. 49

Wang, H., Troxler, T., Yeh, A.-G., and Dai, H.-L. (2000). In Situ, Nonlinear Optical Probe of Surfactant Adsorption on the Surface of Microparticles in Colloids. *Langmuir*, 16(6):2475–2481. Publisher: American Chemical Society. 66, 67, 68, 69, 79

Wang, J. D., Douville, N. J., Takayama, S., and ElSayed, M. (2012). Quantitative Analysis of Molecular Absorption into PDMS Microfluidic Channels. *Annals of Biomedical Engineering*, 40(9):1862–1873. 37, 50

Weber, A. Z., Mench, M. M., Meyers, J. P., Ross, P. N., Gostick, J. T., and Liu, Q. (2011). Redox flow batteries: a review. *J Appl Electrochem*, 41(10):1137. 4

Ying, X., Zhou, H., Hu, J., Xu, Y., Zeng, J., Chen, J., and Kuang, Y. (2009). Electrochemical behavior of K4Fe(CN)6 in [bmim]PF6/TX-100/H2O based microemulsions. *Journal of Applied Electrochemistry*, 39(8):1273–1278. 26

Zhao, Y., Ding, Y., Li, Y., Peng, L., Byon, H. R., Goodenough, J. B., and Yu, G. (2015). A chemistry and material perspective on lithium redox flow batteries towards high-density electrical energy storage. *Chem. Soc. Rev.*, 44(22):7968–7996. Publisher: The Royal Society of Chemistry. 2, 4

Zhu, J., Yu, K., Zhu, Y., Zhu, R., Ye, F., Song, N., and Xu, Y. (2017). Physicochemical properties of deep eutectic solvents formed by choline chloride and phenolic compounds at T=(293.15 to 333.15)K: The influence of electronic effect of substitution group. *Journal of Molecular Liquids*, 232:182–187. 62

# Appendix

# Appendix A

# Appendix

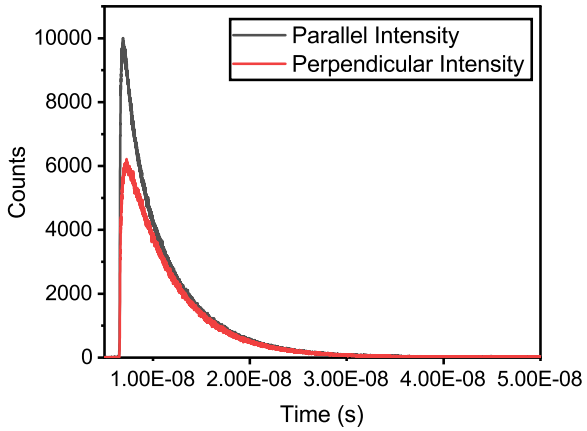


**Figure A.1:** Parallel and perpendicular fluorescence decay of c153 in butanol

**Table A.1:** Summary of Fit Parameters of Fluorescence Anisotropy. Microemulsions are listed by water wt %.

| Probe | $\mu$E* | $r_0$ | $a_1^*$ | $\tau_1$ (ps) | $\tau_2$ (ps) | $\langle\tau\rangle^*$ (ps) |
|---|---|---|---|---|---|---|
| c153 | 10 % | 0.28 | 0.54 | 348.4 ± 30.4 | 1834.6 ± 12.3 | 1033.0 ± 49.7 |
| | 20 % | 0.27 | 0.62 | 332.8 ± 36.6 | 1598.8 ± 55.1 | 814.4 ± 55.5 |
| | 30 % | 0.27 | 0.65 | 307.2 ± 76.5 | 1598.8 ± 250.1 | 716.2 ± 177.4 |
| | 40 % | 0.26 | 0.69 | 279.8 ± 31.1 | 1598.8 ± 107.8 | 610.5 ± 55.9 |
| | 50 % | 0.26 | 0.68 | 232.1 ± 18.0 | 1598.8 ± 98.1 | 511.8 ± 41.1 |
| | 60 % | 0.26 | 0.68 | 221.8 ± 26.0 | 1598.8 ± 180.8 | 489.6 ± 8.66 |
| | 70 % | 0.26 | 0.71 | 233.0 ± 19.8 | 1598.8 ± 153.6 | 484.3 ± 42.9 |
| | 80 % | 0.25 | 0.74 | 233.6 ± 17.1 | 1598.8 ± 194.1 | 514.3 ± 51.4 |
| | 90 % | 0.26 | 0.70 | 273.8 ± 35.4 | 1598.8 ± 215.0 | 605.1 ± 78.5 |
| r6g | 10 % | 0.21 | 1 | 3824.0 ± 85.2 | - | 3824.0 ± 85.3 |
| | 20 % | 0.20 | 1 | 3149.7 ± 209.0 | - | 3149.7 ± 209.0 |
| | 30 % | 0.21 | 1 | 2592.7 ± 132.2 | - | 2592.7 ± 132.2 |
| | 40 % | 0.21 | 1 | 2111.0 ± 95.2 | - | 2111.0 ± 95.2 |
| | 50 % | 0.20 | 1 | 1896.6 ± 123.7 | - | 1896.6 ± 123.7 |
| | 60 % | 0.22 | 1 | 1965.5 ± 107.9 | - | 1965.5 ± 108.0 |
| | 70 % | 0.21 | 1 | 1982.3 ± 238.5 | - | 1982.3 ± 238.5 |
| | 80 % | 0.20 | 1 | 2316.7 ± 136.5 | - | 2316.7 ± 136.5 |
| | 90 % | 0.20 | 1 | 2688.7 ± 238.9 | - | 2688.7 ± 238.9 |
| DPA | 10 % | 0.29 | 0.41 | 629.8 ± 45.5 | 4104.2 ± 117.6 | 2689.8 ± 78.6 |
| | 20 % | 0.32 | 0.51 | 649.0 ± 65.4 | 3797.8 ± 208.7 | 2191.3 ± 96.2 |
| | 30 % | 0.32 | 0.59 | 620.2 ± 26.8 | 3594.2 ± 59.4 | 1842.5 ± 80.2 |
| | 40 % | 0.33 | 0.66 | 586.2 ± 79.3 | 3411.5 ± 319.0 | 1541.5 ± 163.7 |
| | 50 % | 0.32 | 0.68 | 601.0 ± 51.6 | 3324.0 ± 214.0 | 1466.2 ± 106.2 |
| | 60 % | 0.31 | 0.69 | 563.0 ± 35.2 | 3112.9 ± 171.8 | 1352.9 ± 80.3 |
| | 70 % | 0.29 | 0.66 | 591.7 ± 75.2 | 2819.2 ± 229.8 | 1339.9 ± 36.2 |
| | 80 % | 0.26 | 0.57 | 573.8 ± 30.0 | 2560.0 ± 188.0 | 1410.2 ± 47.1 |
| | 90 % | 0.23 | 0.49 | 521.7 ± 26.9 | 2421.0 ± 184.2 | 1497.1 ± 122.7 |

*$\mu$E = Microemulsions
*$a_1$ = 1-$a_2$
*$\langle\tau\rangle = a_1\tau_1 + a_2\tau_2$

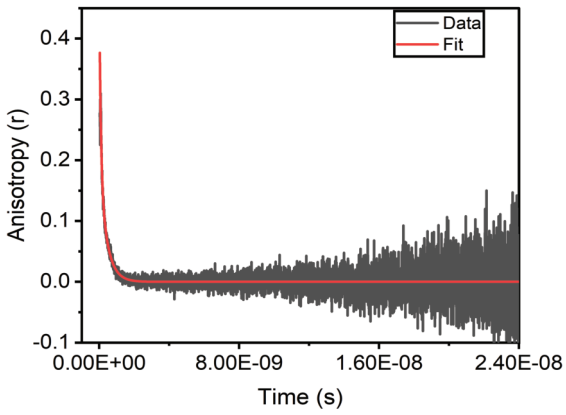


**Figure A.2:** Anisotropy decay of c153 in butanol fitted with biexponential decay curve

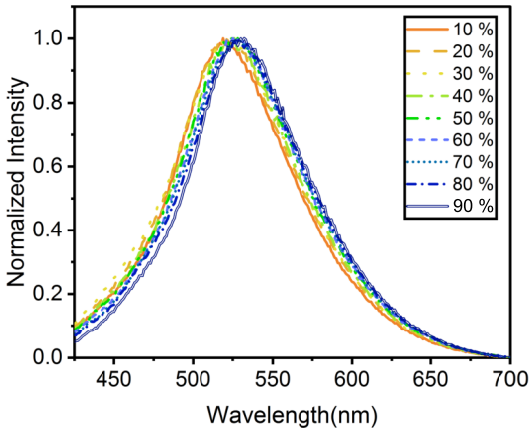


**Figure A.3:** Fluorescence of c153 in microemulsions, with the increase of water percentage in microemulsion the fluorescence maxima red shifts slightly.

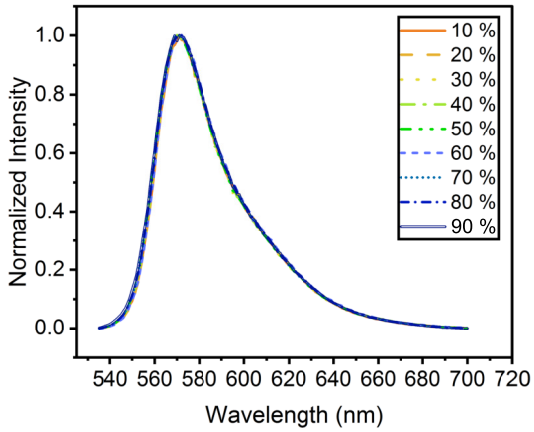


**Figure A.4:** Fluorescence of r6g in microemulsions, the increase of water percentage in microemulsion shows no effect on the fluorescence maxima.

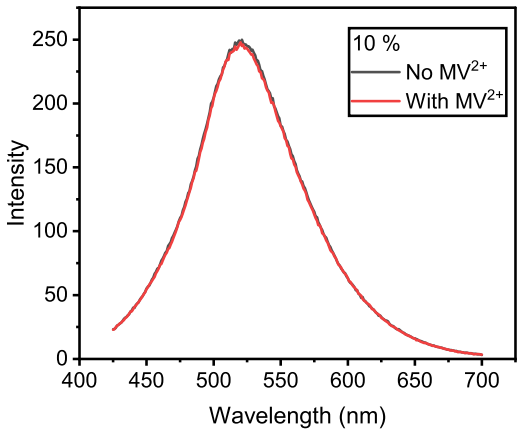


**Figure A.5:** Fluorescence of c153 in 10% microemulsion with and without the presence of MV2+. No photoinduced electron transfer occured as both intesnsities are same.

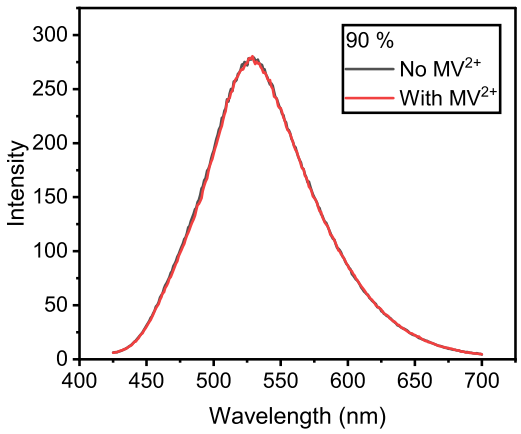


**Figure A.6:** Fluorescence of c153 in 90% microemulsion with and without the presence of MV2+. No photoinduced electron transfer occured as both intesnsities are same.

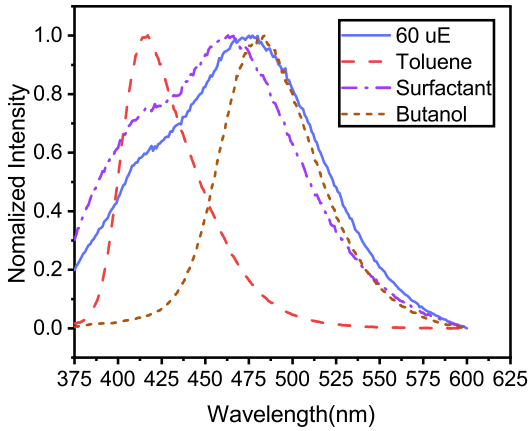


**Figure A.7:** Fluorescence of laurdan in 60 % microemulsions, toluene , surfactant mix, and butanol. The polarity change of the solvent affects the fluorescence of laurdan hence the redshift in maxima.

# Vita

Muhammad Redwan Hassan received his Bachelor of Science degree in Applied Chemistry and Chemical Engineering at the University of Dhaka. He also completed the Master of Science degree in Applied Chemistry and Chemical Engineering at the University of Dhaka. In the fall of 2017, He joined Professor Tessa Calhoun's lab in the Chemistry Department at the University of Tennessee-Knoxville to pursue Ph.D. degree in Chemistry. In December 2022, He completed his Ph.D. degree.